JOURNAL OF COMPUTATIONAL PHYSICS **129,** 263–283 (1996)
ARTICLE NO. 0249

Direct Numerical Simulation of a Turbulent Reactive Plume on a Parallel Computer

Andrew W. Cook and James J. Riley

Department of Mechanical Engineering, University of Washington, Seattle, Washington 98195

Received October 22, 1995; revised May 20, 1996

A computational algorithm is described for direct numerical simulation (DNS) of a reactive plume in spatially evolving grid turbulence. The algorithm uses sixth-order compact differencing in conjunction with a fifth-order compact boundary scheme which has been developed and found to be stable. A compact filtering method is discussed as a means of stabilizing calculations where the viscous/diffusive terms are differenced in their conservative form. This approach serves as an alternative to nonconservative differencing, previously advocated as a means of damping the 2δ waves. In numerically solving the low Mach number equations the time derivative of the density field in the pressure Poisson equation was found to be the most destabilizing part of the calculation. Even-ordered finite difference approximations to this derivative were found to be more stable (allow for larger density gradients) than odd-ordered approximations. Turbulence at the inlet boundary is generated by scanning through an existing three-dimensional field of fully developed turbulence. In scanning through the inlet field, it was found that a high order interpolation, e.g., cubic-spline interpolation, is necessary in order to provide continuous velocity derivatives. Regarding pressure, a Neumann inlet condition combined with a Dirichlet outlet condition was found to work well. The chemistry follows the single-step, irreversible, global reaction: Fuel + (r) Oxidizer $\rightarrow$ (1 + r)Product + Heat, with parameters chosen to match experimental data as far as allowed by resolution constraints. Simulation results are presented for four different cases in order to examine the effects of heat release, Damköhler number, and Arrhenius kinetics on the flow physics. Statistical data from the DNS are compared to theory and wind tunnel data and found in reasonable agreement with regard to growth of turbulent length scales, decay of turbulent kinetic energy, decay of centerline scalar concentration, decrease in scalar rms, and spread of plume profile. Reactive scalar statistics are consistent with expected behavior.

1. INTRODUCTION

Turbulent reacting flows occur in a wide variety of atmospheric, oceanic, and biological processes and, hence, have generated a great deal of scientific interest. Furthermore, the need to predict the combustion efficiency and pollutant formation in a wide variety of man-made devices, from power plants to jet engines, has driven the development of various methods for computing turbulent flows with chemical reactions. The Reynolds number of flows of scientific and engineering interest is often very high; however, many physical phenomena in these flows are also observed in flows at low Reynolds number. Therefore, it is useful and practical to study turbulent reacting flows at lower Reynolds numbers, since such flows can be computed by direct numerical simulation (DNS). In DNS, the exact governing equations are solved in order to gain insight into the turbulence and combustion phenomena. In performing a DNS, it is important to select the proper numerical method for treating the flow of interest. Since turbulent flows contain a wide range of length scales, spectral methods are a natural choice for DNS due to their high accuracy and their ability to correctly represent a broad range of wavenumbers. The application of spectral methods to turbulent reacting flows was initiated by Riley *et al.* [1] and was continued by McMurtry *et al.* [2], Givi *et al.* [3], and Leonard and Hill [4].

Spectral methods are employed by expanding the dependent variables in truncated series of orthogonal basis functions satisfying the required boundary conditions. Spatial derivatives are evaluated locally in the transformed domain, while nonlinear products are evaluated locally in the physical domain. The most common expansion used is Fourier series, although Chebyschev polynomials, Legendre polynomials, Jacobi polynomials, and other series have sometimes been employed [5]. With Fourier methods, the mapping between physical space and spectral space can be performed efficiently using a fast Fourier transform (FFT) algorithm. Spectral and pseudo-spectral methods have the advantages that phase errors are very small and rates of convergence are very high. Pseudo-spectral methods are at least twice as accurate in each spatial dimension as typical finite-difference schemes using the same resolution [6, 7]. One drawback of spectral methods is that the class of complete basis functions, which allow matching the boundary conditions and also possess the properties of rapid convergence, is limited. The application of Fourier series is restricted to problems with periodic or free-slip boundary conditions. Chebyschev polynomials can be applied to problems with arbitrary boundary conditions but the distribution of collocation points for the method may not be ideal for many problems. Spectral methods are thus limited in their ability to treat common boundary

0021-9991/96 $18.00

conditions, e.g., inflow/outflow, although work on the spectral element method [8, 9] has made significant progress in removing this limitation. If spectral methods are applied to flows containing shocks, then the computational grid must be locally refined in order to fully resolve the discontinuity; otherwise Gibb's phenomenon will act to degrade the solution.

Finite-difference methods, on the other hand, have the advantage of easy application to all types of boundary conditions. They may be constructed to arbitrarily high orders of accuracy, albeit with increasing computational cost; hence, second- and fourth-order schemes are most commonly used in computing complex flowfields. In addition, finite-difference schemes have been developed which eliminate spurious oscillations around a shock without the need for smearing the discontinuity over several grid points. E.g., total variation diminishing (TVD) schemes [10] use a "smart" artificial viscosity which is small in regions of smooth flow but which grows at a discontinuity. The growth of the artificial viscosity near the shock reduces the scheme to first-order locally, thereby preventing oscillations.

In treating turbulent reacting flows with heat release it is desirable to have at least one open boundary [11] so that the flow may expand due to chemical heat release [12, 13]. Otherwise, the pressure in the domain will continually increase and affect the turbulence and rate of chemical reaction [2, 14]. This means that a method must be chosen which can accurately resolve the wide range of length scales of the turbulent field, but which can handle open boundary conditions. The compact (Padé) scheme fits both these requirements and therefore is a good choice for computing these types of flows. The sixth-order version of the compact scheme, in particular, provides a high degree of numerical accuracy at a low computational cost. The global nature of the compact scheme makes it necessary to use accurate boundary conditions. Boundary conditions which may seem suitable with low order schemes (with built-in dissipation) may not perform well with compact differencing. The compact scheme is known to work well with nonreflecting boundary conditions [15] which may be used in conjunction with the compressible Navier–Stokes equations. Chen *et al.* [12] used nonreflecting boundary conditions in one direction of an otherwise periodic domain in order to simulate temporally decaying turbulence with an exothermic chemical reaction. Since combustion often occurs at low speeds, a low Mach number approximation is often applied to the fully compressible Navier–Stokes equations in order to increase the maximum stable time step. The resulting equations are elliptic and nonreflecting inflow/outflow conditions can no longer be applied to such flows. One objective of the present work is to demonstrate the stability of the compact scheme with the turbulent inflow/outflow conditions described herein.

Compact schemes have a pure central difference form (except near the boundaries) and thus have no built-in artificial dissipation. This means that they should only be applied to flows where the shortest length scales are determined physically and not numerically; i.e., the solution should be smooth. With finite difference schemes, dispersion errors, resulting from inadequate resolution, show up in local oscillations near a shock or discontinuity. However, since the compact scheme is a global scheme, inadequate resolution in one part of the domain can contaminate the solution everywhere; the same is true for spectral schemes. However, with adequate resolution, the compact scheme is suitable for high Mach number flows and has been used to investigate shock wave structure [16] and to predict shocklet formation in temporally decaying turbulence [17],

In simulating spatially developing turbulence, it is desirable to introduce a fully developed turbulent field at the inlet. Otherwise a lengthy computational region is necessary for instabilities to grow and eventually develop into turbulent flow far downstream [18, 19]. Lee *et al.* [20] introduced a method for generating inlet turbulence in which the energy spectrum of a flow variable is prescribed in terms of frequency and two transverse wave numbers. The Fourier coefficients are written in terms of the prescribed spectrum and a random phase factor. The fluctuation signal is then obtained by inverse Fourier transforms in the homogeneous (transverse) directions, followed by a sum over all frequencies. In order that the signal be nonperiodic, the phase factors are changed once in a given time interval at a random instance and by a random amount. A drawback to this practice is that the generated signal is discontinuous and the frequency spectrum of the turbulence signal generated is not the same as the target spectrum. Furthermore, the incoming flow must undergo some adjustment before the turbulence becomes fully developed. Le and Moin [21] used a modified version of this method to simulate a turbulent, wall-bounded flow over a backward-facing step. Friedrich and Arnal [22] used a different approach in their large eddy simulations (LES) of turbulent flow over a backstep. They first performed a preliminary LES of fully developed channel flow with periodic boundary conditions in the streamwise direction. In the preliminary simulation, they chose a plane perpendicular to the mean flow and stored the velocity vector in that plane for all time steps needed. The stored data were then used as inflow conditions for the backward-facing step flow. A primary motivation for the present work is to test an alternative methodology for introducing a turbulent flow at the inlet. The particular flow under investigation is a reactive plume in spatially evolving grid turbulence. The grid turbulence is specified at the inlet by literal application of Taylor's hypothesis [23] in which a frozen turbulent field is scanned at a rate equal to the mean streamwise velocity.

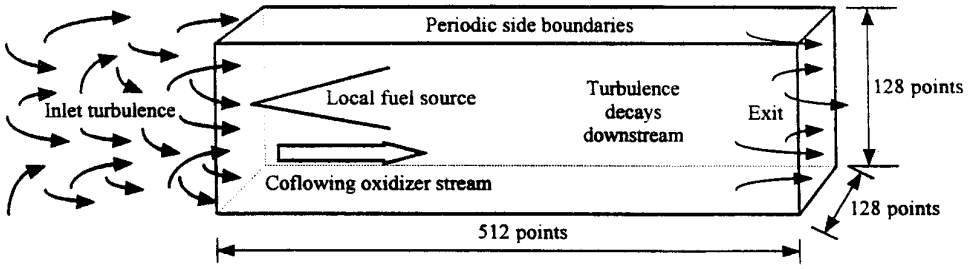

FIG. 1. Schematic of flow geometry.

In the present simulations, a local source of fuel and a coflow of oxidizer are introduced at the inlet along with a fully developed turbulent field. The turbulent flow is designed to match wind tunnel experiments of a plume in grid-generated turbulence. Such experiments have been performed by Mickelsen [24], Gad-el-Hak and Morton [25], Nakamura, Sakai, and Miyata [26], and Brown and Bilger [27]. The fuel reacts with the oxidizer and releases heat as the reactants and product are carried downstream. The nature of the computational algorithm, along with the large memory requirements of the flow configuration, make this problem a good candidate for parallel execution. Hence, a secondary goal of this work is to address key issues involved in parallelizing a DNS code for turbulent reacting flows. In the remaining sections the flow geometry is described and the governing equations are derived. The numerical algorithm is presented in detail, including a description of the inlet boundary condition where the turbulence is introduced. Issues related to parallelizing the code are addressed. A comparison is made between the flow parameters of the DNS and the wind tunnel experiment of Brown and Bilger. Attention is given to the limits of DNS for matching "real-world" flows. Results are presented for the velocity and chemical fields and comparisons are made with various theories and experimental data in order to test the validity of the DNS results. Finally, the effectiveness of the current scheme for computing spatially developing, turbulent, reacting flows is discussed.

2. FLOW CONFIGURATION

The flow to be simulated is a plume, reacting in grid turbulence at low Mach number. The fuel is introduced as a small circular source with a rounded, approximately top-hat profile located at the center of the inlet. The reaction progresses downstream as the turbulence decays. The numerical resolution consists of 512 points in the streamwise direction, with 128 points in each of the transverse directions. The flow is periodic at the cross-stream boundaries with inflow and outflow conditions in the streamwise direction; Fig. 1 shows the flow geometry.

3. NONDIMENSIONALIZATION

In this work, a superscript * denotes a dimensional quantity while a subscript ∞ denotes a free-stream or reference quantity (also dimensional). Subscripts f, o, and p denote the fuel, oxidizer, and product, respectively, in the single-step global reaction: Fuel + (r)Oxidizer $\rightarrow$ $(1 + r)$Product + Heat. Here r is the mass of oxidizer required to react with a unit mass of fuel. Reference and nondimensional quantities are defined as follows:

$L_\infty \equiv$ width of flow domain

$\rho_\infty \equiv$ density at inlet

$U_\infty \equiv$ mean streamwise velocity at inlet

$\mu_\infty \equiv$ dynamic viscosity at inlet

$T_\infty \equiv$ temperature at inlet

$R_\infty \equiv R_u^* \sum_{i=1}^{N} (Y_i/W_i^*) \equiv$ mass-based ideal gas constant

$k^* \equiv$ thermal conductivity

$K^* \equiv$ reaction rate coefficient (depends on Y_{f1} and Y_{o2})

$R_u^* \equiv$ universal gas constant

$E_a^* \equiv$ activation energy

$W_i^* \equiv$ molecular weight of species i

$x_i \equiv x_i^*/L_\infty =$ nondimensional distance in ith distance

$t \equiv U_\infty t^*/L_\infty =$ nondimensional time

$\rho \equiv \rho^*/\rho_\infty =$ nondimensional density

$u_i \equiv u_i^*/U_\infty = i$th component of nondimensional velocity vector **u**

$p \equiv p^*/\rho_\infty U_\infty^2 =$ nondimensional pressure

$T \equiv T^*/T_\infty =$ nondimensional temperature

$\mu \equiv \mu^*/\mu_\infty =$ nondimensional dynamic viscosity

$D_i \equiv D_i^*/D_\infty =$ nondimensional diffusivity of species i

$T_a \equiv E_a^*/R_u^* T_\infty =$ nondimensional activation temperature

$E \equiv p/\rho(\gamma - 1) + u_j u_j/2 =$ nondimensional total energy

$Y_i \equiv$ mass fraction of species i

$Y_{f1} \equiv$ mass fraction of fuel in fuel stream

$Y_{o2} \equiv$ mass fraction of oxidant in oxidizer stream

$\gamma \equiv c_p^*/c_v^* =$ ratio of specific heats

$h_i \equiv h_i^*/R_\infty T_\infty =$ nondimensional enthalpy of formation of species i

$\mathrm{M} \equiv U_\infty/\sqrt{\gamma R_\infty T_\infty} =$ Mach number

$\mathrm{Re} \equiv \rho_\infty U_\infty L_\infty/\mu_\infty =$ Reynolds number

$\mathrm{Pr} \equiv c_p^* \mu^*/k^* =$ Prandtl number (assumed constant)

$\mathrm{Sc} \equiv \mu_\infty/\rho_\infty D_\infty =$ Schmidt number

$\mathrm{Da} \equiv \rho_\infty K^* L_\infty/U_\infty =$ Damköhler number

$\mathrm{Pe} \equiv \mathrm{ReSc} =$ Peclet number

$\mathrm{Le} \equiv \mathrm{Sc/Pr} =$ Lewis number

4. CONSERVATION LAWS

The flow is governed by the Navier–Stokes equations, two species of transport equations, and the ideal gas law. These equations can be written in nondimensional form for a Cartesian coordinate system as

$$\frac{\partial \rho}{\partial t} + \frac{\partial \rho u_j}{\partial x_j} = 0 \tag{1}$$

$$\frac{\partial \rho u_i}{\partial t} + \frac{\partial \rho u_i u_j}{\partial x_j} = -\frac{\partial p}{\partial x_i} + \frac{1}{\mathrm{Re}} \frac{\partial \tau_{ij}}{\partial x_j} \tag{2}$$

$$\frac{\partial \rho E}{\partial t} + \frac{\partial (\rho E + p) u_j}{\partial x_j} = \frac{1}{\mathrm{Re}} \frac{\partial u_l \tau_{jl}}{\partial x_j} + \frac{1}{\mathrm{M}^2 \mathrm{RePr}} \frac{\partial}{\partial x_j} \left(\frac{\mu}{(\gamma - 1)} \frac{\partial T}{\partial x_j} \right) + \frac{q}{\gamma \mathrm{M}^2} \dot{w}_f \tag{3}$$

$$\frac{\partial \rho Y_f}{\partial t} + \frac{\partial \rho Y_f u_j}{\partial x_j} = \frac{1}{\mathrm{ReSc}} \frac{\partial}{\partial x_j} \left(\rho D_f \frac{\partial Y_f}{\partial x_j} \right) - \dot{w}_f \tag{4}$$

$$\frac{\partial \rho Y_o}{\partial t} + \frac{\partial \rho Y_o u_j}{\partial x_j} = \frac{1}{\mathrm{ReSc}} \frac{\partial}{\partial x_j} \left(\rho D_o \frac{\partial Y_o}{\partial x_j} \right) - \dot{w}_o \tag{5}$$

$$p = \frac{\rho T}{\gamma M^2}, \tag{6}$$

where

$$\tau_{ij} = \mu \left(\frac{\partial u_i}{\partial x_j} + \frac{\partial u_j}{\partial x_i} - \frac{2}{3} \delta_{ij} \frac{\partial u_k}{\partial x_k} \right) \quad \text{is the viscous stress tensor} \tag{7}$$

$$\mu = C_1 \frac{T^{3/2}}{T + C_2}, \quad C_1 = 1.3702213, \quad C_2 = 0.3702213 \tag{8}$$

$$\dot{w}_f = Da \rho Y_f \rho Y_o e^{-(T_a/T)} \quad \text{is the reaction rate} \tag{9}$$

$$\dot{w}_o = r \dot{w}_f \tag{10}$$

$$q = h_f + r h_o - (r + 1) h_p \quad \text{is the heat of combustion.} \tag{11}$$

Equations (1)–(3) describe the conservation of mass, momentum, and energy in a fluid continuum. Equations (4) and (5) describe the advection, diffusion, and reaction of fuel and oxidizer, respectively. Equation (6) is the perfect gas law. Here it has been assumed that the fuel, oxidizer, and product are of equal molecular weight, so that a single, apparent gas constant governs the mixture. For turbulent reacting flows with large heat release and chemical species of nonequal molecular weight, the apparent gas constant must be computed as a function of space and time by summing the gas constants of the individual species times their mass fractions. In cases where the reactants are sufficiently dilute, the heat release from the chemical reaction may be insufficient to cause significant density variations; hence the assumption of equal molecular weights need not be made. Equation (8) is Sutherland's empirical formula for the temperature dependence of the dynamic viscosity. The constants C_1 and C_2 correspond to air; hence, it is assumed that air is the primary dilutant. Once combined with a set of boundary and initial conditions, these equations define the mathematical problem to be solved.

5. SCALAR-BASED CHEMISTRY

A mixture-fraction is defined as

$$\xi \equiv \frac{Y_f - Y_o/r + Y_{o2}/r}{Y_{f1} + Y_{o2}/r}. \tag{12}$$

The diffusivity of each of the reacting species is assumed to be equal, so that ξ is a conserved scalar and (5) is replaced in the mathematical problem by

$$\frac{\partial \rho \xi}{\partial t} + \frac{\partial \rho \xi u_j}{\partial x_j} = \frac{1}{\mathrm{ReSc}} \frac{\partial}{\partial x_j} \left(\mu \frac{\partial \xi}{\partial x_j} \right). \tag{13}$$

The mass fractions of oxidizer and product are related to Y_f and ξ via

$$Y_o = Y_{o2}(1 - \xi) + r(Y_f - \xi Y_{f1}) \tag{14}$$

$$Y_p = (r + 1)(\xi Y_{f1} - Y_f). \tag{15}$$

The switch from an oxidizer equation to a conserved scalar equation is motivated by the simpler form and also by theoretical work, such as equilibrium theory [28], the laminar flamelet model [29], and the conditional moment closure [30], which attempt to model average mass fractions and/or reaction rates in terms of Zeldovich parameters

such as ξ. Using this approach, the resulting data more readily allow for comparison with these models. In addition, certain theoretical considerations make use of the stoichiometric surface, which is defined as

$$\xi(\mathbf{x}, t) = \xi_{st} \equiv \frac{Y_{o2}}{rY_{f1} + Y_{o2}}. \tag{16}$$

6. LOW MACH NUMBER APPROXIMATION

Many important reacting flows, ranging from the fate of ozone in the atmosphere to the burning of fossil fuels for energy, occur at low speeds. The Mach number of these flows is small yet the density may vary due to heat release. Explicit numerical methods for computing compressible flows must be able to track the maximum speed at which information may propagate, which is equal to the maximum flow velocity plus the speed of sound. The inviscid CFL condition,

$$\Delta t \le \left(\frac{|u|}{\Delta x} + \frac{|v|}{\Delta y} + \frac{|w|}{\Delta z} + \frac{1}{M}\sqrt{\frac{1}{(\Delta x)^2} + \frac{1}{(\Delta y)^2} + \frac{1}{(\Delta z)^2}} \right)^{-1}, \tag{17}$$

specifies an upper limit to the maximum stable time step that may be used in any explicit method for solving the compressible Navier Stokes (N-S) equations [31]. From this condition we observe that Δt approaches zero as the Mach number goes to zero. Implicit methods permit a larger Δt, but the maximum value is normally less than 5–10 times that given by (17) because, with larger Δt, truncation errors become unacceptable and the time accuracy is lost. Thus, even if an implicit scheme is used, it is not practical to compute very low Mach number flows using the fully compressible N-S equations. This timestep restriction may be circumvented by applying a low Mach number approximation to the governing equations, which effectively decouples the acoustic modes from the vorticity and entropy modes, thus permitting much larger time steps [2]. This makes it much more practical to solve problems where compressibility is primarily due to the exothermicity of chemical reactions, which is the case considered here. The low Mach number approximation is useful in reacting flows if the chemistry is not too fast. Otherwise it may be the fastest reaction, and not the fluid velocity, that sets the maximum stable timestep. Furthermore, if the reaction is too strong, a high Mach number, e.g., detonation, flow may develop.

The low Mach number equations are derived as follows: Let $\varepsilon \equiv \gamma \mathrm{M}^2 \ll 1$ and expand the dependent variables as power series in ε:

$$\rho = \rho^{(0)} + \varepsilon\rho^{(1)} + \cdots \tag{18}$$

$$u_i = u_i^{(0)} + \varepsilon u_i^{(1)} + \cdots \tag{19}$$

$$T = T^{(0)} + \varepsilon T^{(0)} + \cdots \tag{20}$$

$$p = \frac{\rho T}{\gamma M^2} = \frac{1}{\varepsilon}\rho^{(0)}T^{(0)} + \rho^{(1)}T^{(0)} + \rho^{(0)}T^{(1)} + \cdots = \frac{1}{\varepsilon}p^{(0)} + p^{(1)} + \cdots \tag{21}$$

$$\rho E = \frac{p}{\gamma - 1} + \rho\frac{u_j^2}{2} = \frac{1}{\varepsilon}\frac{p^{(0)}}{\gamma - 1} + \frac{p^{(1)}}{\gamma - 1} + \rho^{(0)}\frac{u_j^{(0)2}}{2} + \cdots \tag{22}$$

$$\xi = \xi^{(0)} + \varepsilon\xi^{(0)} + \cdots \tag{23}$$

$$Y_f = Y_f^{(0)} + \varepsilon Y_f^{(1)} + \cdots. \tag{24}$$

Substituting Eqs. (18)–(24) into Eqs. (1)–(4), (6), and (13) and collecting the lowest order terms in ε, yields the following first-order equations:

$$\frac{\partial\rho^{(0)}}{\partial t} + \frac{\partial\rho^{(0)}u_j^{(0)}}{\partial x_j} = 0 \tag{25}$$

$$\frac{\partial p^{(0)}}{\partial x_i} = 0 \tag{26}$$

$$\rho^{(0)}\frac{\partial u_j^{(0)}}{\partial x_j} = \frac{1}{T^{(0)}}\left[\frac{1}{\mathrm{RePr}}\frac{\partial}{\partial x_j}\left(\mu\frac{\partial T^{(0)}}{\partial x_j}\right) + \frac{\gamma - 1}{\gamma}q\dot{w}_f\right] \tag{27}$$

$$\frac{\partial\rho^{(0)}\xi^{(0)}}{\partial t} + \frac{\partial\rho^{(0)}\xi^{(0)}u_j^{(0)}}{\partial x_j} = \frac{1}{\mathrm{ReSc}}\frac{\partial}{\partial x_j}\left(\mu\frac{\partial\xi^{(0)}}{\partial x_j}\right) \tag{28}$$

$$\frac{\partial\rho^{(0)}Y_f^{(0)}}{\partial t} + \frac{\partial\rho^{(0)}Y_j^{(0)}u_j^{(0)}}{\partial x_j} = \frac{1}{\mathrm{ReSc}}\frac{\partial}{\partial x_j}\left(\mu\frac{\partial Y_f^{(0)}}{\partial x_j}\right) - \dot{w}_f \tag{29}$$

$$p^{(0)} = \rho^{(0)}T^{(0)}. \tag{30}$$

Equation (26) states that $p^{(0)}$, which is interpreted as the thermodynamic pressure, is uniform in space. Thus, for combustion in an open domain, $p^{(0)}$ is fixed to its value at ∞, which is here assumed to be constant in time. Thus (27), the lowest order energy equation, contains no time derivative. Note that heating due to viscous dissipation drops out as a result of the approximation and that (25), (28), and (29) remain unchanged.

Since all the dependent variables except $p^{(0)}$ have dropped out of the first-order momentum equation, the second-order momentum equation must be included in order to close the system:

$$\frac{\partial\rho^{(0)}u_i^{(0)}}{\partial t} + \frac{\partial\rho^{(0)}u_i^{(0)}u_j^{(0)}}{\partial x_j} = -\frac{\partial p^{(1)}}{\partial x_i} + \frac{1}{\mathrm{Re}}\frac{\partial\tau_{ij}^{(0)}}{\partial x_j}. \tag{31}$$

Here, $p^{(1)}$ is interpreted as the dynamic pressure. Since $p^{(0)} = \text{const}$, (25), (27), (28)–(31) comprise eight equations for the eight unknowns: $\rho^{(0)}$, $u^{(0)}$, $v^{(0)}$, $w^{(0)}$, $T^{(0)}$, $p^{(1)}$, $\xi^{(0)}$, and $Y_f^{(0)}$; thus, the equation set is closed.

7. NUMERICAL ALGORITHM

7.1. *Third-Order Adams–Bashforth Scheme*

The superscripts will now be dropped, except to distinguish between the thermodynamic, $p^{(0)}$, and dynamic, $p^{(1)}$, pressures. Integrating Eq. (31) from time t to time $t + \Delta t$ gives

$$(\rho u_i)^{n+1} - (\rho u_i)^n = \int_t^{t+\Delta t} B_i \, dt - \frac{\partial}{\partial x_i} \Delta t \mathscr{P}, \tag{32}$$

where

$n = t/\Delta t$

$B_i = (\partial/\partial x_j)(\tau_{ij}/\mathrm{Re}) - (\rho u_i u_j)$

$\mathscr{P}$ = dynamic pressure averaged over time interval $(t, t + \Delta t)$.

The integral on the right-hand side of (32) is computed using a third-order, one-sided approximation,

$$\int_t^{t+\Delta t} B_i \, dt = \frac{\Delta t}{12} (23 B_i^n - 16 B_i^{n-1} + 5 B_i^{n-2}), \tag{33}$$

which, when used in (32), gives the Adams–Bashforth (A-B) scheme. The A-B method is numerically efficient, but requires fluxes at two previous time-steps and, thus, has large storage requirements [32]. This scheme is well suited to the CM-5 which has 16 Gbytes of RAM. Taking the divergence of (32) and using (25) gives

$$\nabla^2 \mathscr{P} = \frac{1}{\Delta t} \left[\left(\frac{\partial \rho}{\partial t} \right)^{n+1} + \nabla \cdot (\rho \mathbf{u})^* \right], \tag{34}$$

where

$$(\rho u_i)^* = (\rho u_i)^n + \frac{\Delta t}{12} (23 B_i^n - 16 B_i^{n-1} + 5 B_i^{n-2}). \tag{35}$$

The density time derivative in (34) is a potential source of instability and requires careful treatment. In practice, the second-order explicit approximation

$$\left(\frac{\partial \rho}{\partial t} \right)^{n+1} = \frac{3\rho^{n+1} - 4\rho^n + \rho^{n-1}}{2 \, \Delta t} \tag{36}$$

has been found to be much more stable than third-order explicit and compact approximations, e.g.,

$$\left(\frac{\partial \rho}{\partial t} \right)^{n+1} = 3 F_\rho^n - 3 F_\rho^{n-1} + F_\rho^{n-2}, \tag{37}$$

where F_ρ is defined in Eq. (39) below. This is likely due to the fact that even-ordered schemes are dissipative, whereas odd-ordered schemes are dispersive [31]. Even with an even-ordered approximation to the density time derivative, however, it was found that the third-order Adams–Bashforth scheme is only stable for maximum density variations up to about a factor of 3. Sandoval found that by decreasing the Reynolds number and performing an iteration, larger variations in ρ could be achieved [33]. Najm demonstrated that a predictor–corrector time-stepping algorithm is stable for very large density changes [34].

The momentum equation now becomes

$$(\rho u_i)^{n+1} = (\rho u_i)^* - \Delta t \frac{\partial \mathscr{P}}{\partial x_i}, \tag{38}$$

where $\mathscr{P}$ is the solution to (34) using (36). Finally, heat release and diffusion effects must be included by ensuring that Eq. (27) is satisfied at each instant in the calculation. There are several ways of doing this; here we will follow the technique of McMurtry *et. al.* [2] by rewriting Eq. (25) as

$$\frac{\partial \rho}{\partial t} + u_j \frac{\partial \rho}{\partial x_j} + \rho \frac{\partial u_j}{\partial x_j} = 0$$

and replacing the third term on the left-hand side with Eq. (27). This gives an equation for the local density,

$$\frac{\partial \rho}{\partial t} = F_\rho = -u_j \frac{\partial \rho}{\partial x_j} - \frac{1}{T} \left[\frac{1}{\mathrm{RePr}} \frac{\partial}{\partial x_j} \left(\mu \frac{\partial T}{\partial x_j} \right) + \frac{\gamma - 1}{\gamma} q \dot{w}_f \right]. \tag{39}$$

7.2. *Pressure Projection Method*

The equations are advanced in time according to the projection method [35]. First, Eq. (39) is time-stepped via (33) to obtain ρ^{n+1}, and Eq. (36) is used to get $(\partial \rho/\partial t)^{n+1}$. Second, $(\rho u_i)^*$ is obtained from Eq. (35), $\nabla \cdot (\rho \mathbf{u})^*$ is taken, and the right-hand side of (34) is computed. Third, with periodicity in the y and z directions, Eq. (34) is Fourier transformed in y and z yielding

$$\frac{\partial^2 \hat{\mathscr{P}}}{\partial x^2} - \lambda^2 \hat{\mathscr{P}} - \kappa^2 \hat{\mathscr{P}} = \widehat{\widehat{\mathrm{rhs}}}(x, \lambda, \kappa),$$

where a hat, $\hat{\phi}$, denotes the Fourier transform of a function and λ and κ are wavenumbers in the y and z directions,

respectively. The flow is assumed to exit into a large ambient domain; hence the exit pressure is set to zero. With the exit pressure fixed, a Neumann condition must be supplied at the entrance [36]; hence the pressure derivative normal to the inlet is set to zero. A fourth-order central finite difference approximation for $\partial^2 \hat{\hat{\mathscr{P}}}/\partial x^2$, with a second-order approximation at the $i = 2$ and $i = nx\text{-}1$ boundary nodes, results in the following pentadiagonal matrix for $\hat{\hat{\mathscr{P}}}$:

$$
\begin{aligned}
-3\hat{\hat{\mathscr{P}}}_1 + 4\hat{\hat{\mathscr{P}}}_2 - \hat{\hat{\mathscr{P}}}_3 &= 0 \\
\hat{\hat{\mathscr{P}}}_1 - [2 + \Delta x^2(\lambda^2 + \kappa^2)]\hat{\hat{\mathscr{P}}}_2 + \hat{\hat{\mathscr{P}}}_3 &= \Delta x^2 \,\widehat{\widehat{\mathrm{rhs}}}\,(2, \lambda, \kappa) \\
&\vdots \\
-\hat{\hat{\mathscr{P}}}_{i-2} + 16\hat{\hat{\mathscr{P}}}_{i-1} - [30 + 12\Delta x^2(\lambda^2 + \kappa^2)]\hat{\hat{\mathscr{P}}}_i & \\
+ 16\hat{\hat{\mathscr{P}}}_{i+1} - \hat{\hat{\mathscr{P}}}_{i+2} &= 12\Delta x^2 \,\widehat{\widehat{\mathrm{rhs}}}\,(i, \lambda, \kappa) \\
&\vdots \\
\hat{\hat{\mathscr{P}}}_{nx-2} - [2 + \Delta x^2(\lambda^2 + \kappa^2)]\hat{\hat{\mathscr{P}}}_{nx-1} & \\
+ \hat{\hat{\mathscr{P}}}_{nx} &= \Delta x^2 \,\widehat{\widehat{\mathrm{rhs}}}\,(nx - 1, \lambda, \kappa), \\
\hat{\hat{\mathscr{P}}}_{nx} &= 0.
\end{aligned}
$$

After solving this system of equations for $\hat{\hat{\mathscr{P}}}$, $\mathscr{P}$ is then obtained by a two-dimensional inverse FFT. Next, $\mathscr{P}$ is used in Eq. (38) to get $(\rho u_i)^{n+1}$. Finally, Eqs. (28) and (29) are time-stepped via (33) to get $(\rho\xi)^{n+1}$ and $(\rho Y_f)^{n+1}$, and all primitive variables at time $n + 1$ are obtained by dividing by ρ^{n+1}. Note that $p^{(0)}$ is set from the initially constant density and temperature fields according to (30).

7.3. *Sixth Order Compact Scheme*

The code uses a sixth-order accurate compact scheme for computing spatial derivatives. The compact scheme is superior to finite-difference methods in resolving the small scales. The resolution characteristics of a scheme can be quantified by means of a Fourier analysis of the differencing algorithm. Lele [16] has demonstrated that compact schemes are similar to spectral schemes in accurately computing the higher wavenumbers of a problem. This makes them good alternatives to spectral schemes if the problem has nonperiodic boundaries. Typically the global error is dominated by the boundary error; thus it is desirable to have a high formal accuracy at the boundaries. In the present simulations, a fifth-order compact boundary scheme has been derived for use at the inlet and exit. The fifth-order scheme is one-sided at the first boundary node and ''lop-sided'' at the second boundary node. Combining the sixth-order scheme for the interior points with the fifth-order boundary scheme results in the following tridiagonal matrix for the x derivative, ϕ', of a variable, ϕ:

$$
\begin{aligned}
\phi'_1 + 4\phi'_2 &= -\frac{37}{12h}\phi_1 + \frac{2}{3h}\phi_2 \\
&\quad + \frac{3}{h}\phi_3 - \frac{2}{3h}\phi_4 + \frac{1}{12h}\phi_5 \\
\alpha\phi'_1 + \phi'_2 + \alpha\phi'_3 &= a\phi_1 + b\phi_2 + c\phi_3 + d\phi_4 + g\phi_5 \\
&\vdots \\
12\phi'_{i-1} + 36\phi'_i + 12\phi'_{i+1} &= (\phi_{i+2} + 28\phi_{i+1} \\
&\quad - 28\phi_{i-1} - \phi_{i-2})/h \\
&\vdots \\
\alpha\phi'_{nx-2} + \phi'_{nx-1} + \alpha\phi'_{nx} &= -a\phi_{nx} - b\phi_{nx-1} \\
&\quad - c\phi_{nx-2} - d\phi_{nx-3} - g\phi_{nx-4} \\
4\phi'_{nx-1} + \phi'_{nx} &= \frac{37}{12h}\phi_{nx} - \frac{2}{3h}\phi_{nx-1} \\
&\quad - \frac{3}{h}\phi_{nx-2} + \frac{2}{3h}\phi_{nx-3} - \frac{1}{12h}\phi_{nx-4}.
\end{aligned}
$$

Here:

$h = \Delta x = \Delta y = \Delta z =$ grid spacing
$\alpha = 0.2142857143$
$a = -0.6785714286/h$
$b = -0.119047619/h$
$c = 0.8571428571/h$
$d = -0.07142857143/h$
$g = 0.0119047619/h$.

A periodic tridiagonal solver is used to compute derivatives in the y and z directions. The sixth-order compact scheme has the ability to accurately represent phase speeds at high wavenumbers. The inability of conventional finite-difference schemes to accurately compute phase speeds at high wavenumbers can lead to significant dispersion errors in the solution.

8. BOUNDARY CONDITIONS

The elliptic nature of the equations presents a dilemma since boundary variables depend on uncomputed regions upstream and downstream of the computational domain; thus some error is unavoidable at the inlet and exit.

8.1. *Inlet*

All variables, except pressure, are specified at the inlet. The incoming turbulence is created by ''scanning'' through an existing 128^3 velocity field generated by Mell [37]. The rate of scan is set equal to the mean streamwise velocity

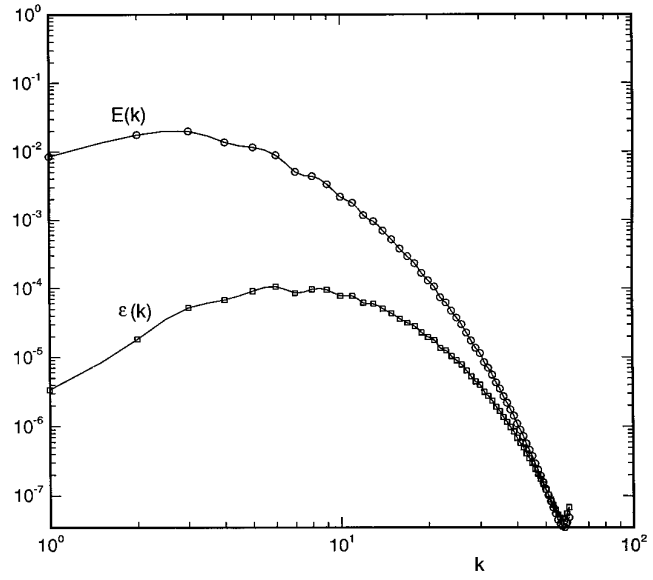

FIG. 2. Three-dimensional energy and dissipation spectra of inlet turbulence.

at the inlet U_∞, and cubic-spline interpolation is used to obtain velocity values which lie between data planes. It was found that linear interpolation is unacceptable since it gives functions with discontinuous derivatives. The pressure-work term in the equation for the conservation of mechanical energy is very sensitive to velocity derivatives at the inlet and linear interpolation causes this term to oscillate.

Figure 2 shows the three-dimensional energy and dissipation-rate spectra of the inlet turbulence, $E(k)$ and $\varepsilon(k)$, respectively, where k is the magnitude of the three-dimensional wavevector. The spectra were computed by averaging the Fourier amplitudes of the velocities over spherical shells in wavenumber space. The integral, Taylor, and Kolmolgorov scales at the inlet are

$$l \equiv \frac{l^*}{L_\infty} = \left(\frac{3}{8}\right) \frac{\int_0^\infty (E(k)/k)\, dk}{\int_0^\infty E(k)\, dk} = 0.141$$

$$\lambda \equiv \frac{\lambda^*}{L_\infty} = \frac{1}{2\pi} \left(\frac{15 u_{\text{rms}}^2}{\int_0^\infty k^2 E(k)\, dk}\right)^{1/2} = 0.0646$$

$$\eta \equiv \frac{\eta^*}{L_\infty} = \frac{1}{2\pi} \left(\frac{1}{15}\right)^{1/4} \left(\frac{\nu\lambda}{\text{Re} u_{\text{rms}}}\right)^{1/2} = 0.00400.$$

Here u_{rms} is the root-mean-square velocity of the incoming turbulence nondimensionalized by U_∞ (i.e., the turbulence level).

8.2. *Exit*

A one-dimensional advection condition is used at the outlet such that all variables, except pressure, satisfy an equation of the form

$$\frac{\partial \phi}{\partial t} + C \frac{\partial \phi}{\partial x} = 0, \tag{40}$$

where C is a phase speed which should characterize the celerity of the large eddies [38] and must be positive for stability [39]. Often C is set to an average exit velocity [40], which is the case here; hence $C = \langle U \rangle_{\text{exit}}$.

9. CONSERVATION CHECKS

Since the continuity equation (1) has been replaced by (39), a valid question arises as to whether the numerical algorithm conserves mass. In performing the simulations, conservation of mass and momentum are periodically checked by integrating the continuity and mechanical energy equations over the flow domain. The scheme was found to conserve both mass and momentum globally. The various terms monitored in the mechanical energy equation are

$$\frac{\partial}{\partial t} \int_V \rho \frac{u_j u_j}{2}\, dV \text{ rate of increase of energy}$$

$$\int_A \rho u \frac{u_j u_j}{2} \Big|_{x_1}^{x_2} dA \text{ net energy flux through inlet and outlet}$$

$$\int_V u_j \frac{\partial \mathscr{P}}{\partial x_j}\, dV \text{ pressure work}$$

$$-\frac{1}{\text{Re}} \int_V u_i \frac{\partial \tau_{ij}}{\partial x_j}\, dV \text{ viscous work.}$$

The terms should sum to zero if momentum is conserved. If the Reynolds number is increased beyond that which allows adequate resolution, the sum of these terms will deviate from zero. This effect shows up well before the solution becomes unstable and provides a resolution check on the simulation. Additionally, the left- and right-hand sides of the internal energy equation (27) and the Poisson equation (34) are periodically compared and plotted. These relations were found to be satisfied at each instant in the calculation, ensuring conservation of energy and an accurate dynamic pressure field. The agreement between the left- and right-hand sides of these equations is quantified by calculating a normalized difference defined as

$$\Theta \equiv \frac{\langle (\text{LHS} - \text{RHS})^2 \rangle}{\sqrt{\langle (\text{LHS})^2 \rangle \langle (\text{RHS})^2 \rangle}},$$

where Θ must be close to zero for a well-resolved calculation.

10. STABILITY

The stability of the compact scheme depends on the manner in which second derivatives are computed. Note that, in the viscous/diffusive terms in the governing equations, μ, ρ and D are not constants and appear inside one of the derivatives. This means that it is much simpler to compute a first derivative, multiply it by the appropriate variable(s), and then take another derivative, than it is to expand the derivatives using the chain rule and then take second derivatives directly. Furthermore, expanding the viscous/diffusive terms causes the loss of their conservative form. However, Lele [16] advocates using the nonconservative approach in order to provide finite damping of grid to grid oscillations (2δ waves). The 2δ waves remain undamped if the conservative form is used with two consecutive applications of the first derivative operator. This means that tiny oscillations, possibly arising from numerical roundoff error, may gradually grow in time and eventually affect the stability of the scheme.

In the present approach the viscous/diffusive terms are solved in conservative form. Damping the 2δ waves is accomplished by a applying a fourth-order compact filter to the primitive variables at every fifth timestep. The energy removed by the filter is compared to the other terms in the integrated mechanical energy equation and found to be negligible. Compact filters are much better low pass filters than explicit schemes since they confine their effects to the highest wavenumbers. This provides the necessary damping of the 2δ waves without contaminating the computation. However, filtering in this manner will not stabilize an underresolved calculation [41].

11. PARALLEL COMPUTING

11.1 *Optimization*

The primary task of converting a code to run on a distributed memory machine is to optimize array layouts in memory so that the computational load is well balanced among the processors. Another task is to minimize interprocessor communication which necessarily results from finite-difference operations. On the CM-5, each element of an array may reside on a different virtual processor or the entire array may reside on the front-end computer. The manner in which array elements are distributed among the processors can have tremendous impact on the performance of a DNS code. In order to achieve good performance, it is crucial that order-dependent operations (do loops) be avoided wherever possible and that they not be performed on array indices that have been distributed over multiple nodes. Such operations force all but one processor to sit idle until the operation is complete. By optimizing array layouts in memory, the execution time of the present code was decreased by over a factor of 30.

The Poisson solver described previously, as well as the compact scheme for computing spatial derivatives, both require matrix inversions. The Gaussian reduction procedure for matrix inversion is necessarily an order-dependent process. One method for parallelizing matrix operations is to split the matrix into submatricies and follow a fork-and-join model [42], where each processor is given some number of operations to perform. For the present simulations, a much simpler approach, i.e., domain decomposition, was taken. For example, in order to to compute the x derivative of an array, the array is first copied into a dummy array with the x dimension laid out serially so that all elements of the x index reside on a single processor. The Gaussian reduction operation is then done serially on that index. Since the computational domain is three dimensional, the matrix inversion along the x direction is done a plane at a time, i.e., the domain is partitioned into y-z planes which are operated on in parallel. This practice is most efficient if the total number of grid points in a y-z plane equals or exceeds the number of physical processors available. In such cases, no penalty is paid by executing the x index serially. The same procedure is used for computing y and z derivatives. Layout changes of this sort require extensive node communication, but this is a relatively efficient process on the CM-5; i.e., it is far faster than performing a do loop operation on an array index which has been distributed over multiple nodes. Fast Fourier transforms (FFTs) may operate on the same principle, transforming in one direction a plane at a time. If a purely serial operation must be performed, i.e., one that cannot be parallelized in any direction, then the quickest procedure is to call a library routine which copies the array onto the front-end computer, operate on the array, and then call another library routine to copy the results back to the CM. However, on the CM-5, caution must be taken to ensure that there are no array home mismatches. An array home mismatch occurs whenever an array is passed to a subroutine in which it has a different layout than in the calling routine. If this happens, the code will run, but the computed results will be in error.

11.2. *Performance*

One measure of the parallel efficiency of a code is how evenly the computational load is distributed among the processors. For the present simulations the load balance was measured as follows:

$$\text{Load balance} = \frac{(\text{Total node} + \text{Communication time})}{(\text{Number of processors})(\text{Total elapsed time})} = 0.91.$$

If all of the processors are busy all of the time, then the above ratio will be unity. If many processors sit idle while only a few are computing, then this ratio will be much lower. The ratio for the plume code of 0.91 indicates a reasonably efficient use of all processors. The efficient use of processors is aided by choosing grid dimensions which match the number of processors in a partition. E.g., if the code is run on a 128-node partition, then a grid resolution of 128 points, or some multiple thereof in at least one direction, is optimal.

Another measure of parallel efficiency is scalability, i.e., the reduction in computing time achieved when the number of processors is doubled. If the amount of interprocessor communication of a code is very high, it will not perform well on a large processor partition. For the present code, wall clock times were measured on two different partitions (using a grid resolution of $512 \times 128 \times 128$) to obtain the following measure of scalability:

$$\text{Scalability} = \frac{43.8 \text{ s per time-step on 128-node partition}}{24.3 \text{ s per time-step on 256-node partition}} = 1.8.$$

The scalability factor of 1.8 again indicates a well-parallelized code. The memory requirements of the code increase slightly as the number of processors increases. Running on a 128-node partition requires 2.75 Gbytes of RAM, whereas running on a 256-node partition requires 3 Gbytes. This may be due to the way the compiler optimizes the code for different partitions.

Using standard linear equations software, comparisons have been made of actual floating-point operations per second achieved, using full optimization, on both the CM-5 and Cray C90 [42]. A Cray C90 with 16 processors with cycle times of 4.2 ns ran the computer code at 10.78 Gflops, whereas a CM-5 with 512 processors ran at 30.4 Gflops. However, the operational speed of the computers depends to a large extent on the nature and size of the computations performed, and these numbers should not be taken as an absolute measure of the machines relative performance. For the present simulations, the CM-5 was chosen for its large amount of memory.

12. SIMULATION PARAMETERS

Four different simulations were performed which will be denoted by the letters A, B, C, and D. Case A was designed to match the reactive plume experiment of Brown and Bilger [27] to the extent possible. In their experiment, the reacting species concentrations were very small so that the effects of heat release could be neglected and, hence, the flow was incompressible. Therefore, the heat release q and activation temperature T_a in the DNS case A were set to zero. Note that Brown and Bilger work with molar fractions, whereas here mass fractions are used. Table I lists parameters for the wind tunnel experiment and for case A from the numerical simulation. In the table, d is the nozzle diameter of the fuel source (for the DNS this is defined as the diameter of a tophat source having equivalent mass flux), and Da_t and Re_t are the turbulent Damköhler and Reynolds numbers, respectively, defined at the inlet. The parameters d/l and Re_t differ due to numerical resolution requirements.

TABLE I

Comparison of Flow Parameters from the Wind Tunnel Experiment of Brown and Bilger and from the DNS Case A

Parameter	Experiment	DNS case A
$u_{\mathrm{rms}} \equiv \left(\frac{\{\mathbf{u}\cdot\mathbf{u}\rangle}{3}\right)^{1/2}$	0.062	0.26
$\frac{d}{l}$	0.185	0.642
r	1.6	1.6
Y_{o2}	1.67×10^{-6}	0.2
Y_{f1}	5.52×10^{-4}	1
$\xi_{\mathrm{st}} \equiv \frac{Y_{o2}}{rY_{f1} + Y_{o2}}$	0.00184	0.111
$\mathrm{Da}_t \equiv \frac{K^* l^*}{u^*_{\mathrm{rms}}}$	3.81	3.81
$\mathrm{Re}_t \equiv \frac{u^*_{\mathrm{rms}} l^*}{\nu^*}$	665	147
Sc	0.75	0.75

Regarding the difference in ξ_{st}, very low values of ξ_{st} act to increase the resolution requirements of the chemical fields. This can be understood by considering the resolution requirements for Y_p. Y_p is zero where ξ is zero, and it attains its maximum value, where $\xi = \xi_{\mathrm{st}}$. If ξ_{st} is close to zero, then a small change in ξ corresponds to a very large change in Y_p. The same is true for Y_o, which must be adequately resolved in order to get accurate values for $\dot{w}_f$. The fact that an equation for Y_o is not being solved makes no difference since small errors f in Y_f and ξ translate into large errors for Y_o, i.e., through Eq. (14). In other words, the frozen and equilibrium limits for $Y_f(\xi)$ become very close together. This is the reason for the differences in Y_{f1}, Y_{o2}, and, hence, ξ_{st}, between the experiment and the DNS. The resolution difficulties associated with very small (or very large) values of ξ_{st} are not widely recognized.

The reason for the difference in u_{rms} requires some explanation. In order to get a complete picture of the combustion process, the computation is carried far enough downstream so that the reaction reaches completion, i.e., the fuel is nearly all consumed. This requires vast computer resources and so it is desirable to shrink the required distance as much as possible. This is accomplished by making u_{rms} large (or, equivalently, U_∞ smaller compared to u^*_{rms}); how-

TABLE II

Parameters That Varied from Case to Case in the Numerical Simulations

Parameter	A	B	C	D
q	0	73.03	73.03	224.7
Da_t	3.81	3.81	16.3	3.81
T_a	0	0	3	3

Note. Number, Pr = Sc = 0.75, and all other flow parameters remained as stated in Table I.

ever, stability dictates that there be no backflow through the inlet, which effectively sets the maximum value of u_{rms} such that at any given time the minimum streamwise velocity at the inlet is greater than or equal to zero. This practice results in a higher turbulence level than that found in most wind tunnel experiments. Thus some comparisons with laboratory data are made by interpreting both sets of data using a frame of reference moving with $\langle U\rangle$. This is accomplished by considering the time $t = x/\langle U\rangle$ and defining the initial large eddy turnover time as $\tau = l/u_{\mathrm{rms}}$, so that the downstream large-eddy time is defined as $t_{\mathrm{le}} = t/\tau = xu_{\mathrm{rms}}/\langle U\rangle l$. The number of large eddy turnovers is thus proportional to $u_{\mathrm{rms}}/\langle U\rangle$. Note that if this ratio is not much less than one, then the integral scale of the turbulence is of the order of the longitudinal scale of decay and, hence, homogeneity in the streamwise direction may not be assumed [43].

Cases B, C, and D were performed in order to examine the effects of heat release, activation temperature, and the Damköhler number on the reaction physics. Table II lists the parameters that were varied from case to case. In all cases, the Prandtl number was equal to the Schmidt number, Pr = Sc = 0.75, and all other flow parameters remained as stated in Table I.

13. VISUALIZATION

Figure 3, taken from case D, shows instantaneous contours of density, vorticity-magnitude, mixture-fraction, and reaction rate on a planar slice down the centerline of the plume; the flow enters at the left and exits to the right. The plots were made at the end of the simulation, after all variables had reached statistical stationarity. Since the fuel is in short supply, the reaction rate is strongest near the inlet where fuel is in greatest abundance. Figure 4 shows instantaneous "head on" views of ξ at various downstream locations including the inlet. The plots, taken from case A, demonstrate how the initially circular plume is rapidly distorted by the turbulence and eventually reaches the side boundaries.

14. RESULTS

14.1. *Turbulent Flow Field*

Since the domain is periodic in the transverse directions, two-dimensional energy spectra can be calculated by Fourier transform in y and z. Figure 5 shows instantaneous 2D total energy spectra of the velocity field at various downstream locations for case A, where k_2 is the magnitude of the 2D wavevector. The spectra were computed by transforming planar (y-z) sections of u, v, and w at an instant in time and averaging over annular sections in Fourier space. Two-dimensional spectra are seldom measured in experiments but are sometimes computed from DNS [44] when there are only two periodic directions. The spectra provide a check on the numerical resolution, which is seen to be very good. Figure 6 shows longitudinal autocorrelations of velocity at various downstream locations for case A. In addition to being temporally stationary, the turbulence is spatially homogeneous in y and z; hence, averages are computed over time and over cross-stream directions. The correlation function f is defined below for the transverse components of velocity, with the averaging procedure shown to the right of each equation,

$$f_v(\Delta y) = \frac{\langle v(t,x,y,z)v(t,x,y+\Delta y,z)\rangle}{\langle v(t,x,y,z)^2\rangle}, \quad \langle(\,)\rangle \equiv \int_0^1\int_0^1 (\,)\,dz\,dt, \tag{41}$$

$$f_w(\Delta z) = \frac{\langle w(t,x,y,z)w(t,x,y,z+\Delta z)\rangle}{\langle w(t,x,y,z)^2\rangle}, \quad \langle(\,)\rangle \equiv \int_0^1\int_0^1 (\,)\,dy\,dt. \tag{42}$$

Far downstream, the tails of the curves rise above zero as the integral scale of the turbulence, l^*, approaches the lateral length of the computational domain, L_∞. Theoretically, the curves for v and w should be indentical and symmetric. The lack of equality and symmetry gives some idea of the statistical errors. The statistical errors are due to the finite time and finite space samples of the data. Since the inlet turbulence is periodic, the time signal repeats itself and, hence, there are a limited number of statistically independent samples available. If the length of the turbulent field being fed through the inlet were increased, then the statistical errors would decrease.

In Fig. 7 the mean density is plotted as a function of downstream distance for the three cases with heat release. Here the density was averaged in time and over the cross-stream directions y and z. In Fig. 8 the rms density normalized by the mean density is plotted. Case B differs from cases C and D due to the difference in T_a. Higher activation temperatures slow the reaction, thereby decreasing the rate of heat release and density dilatation.

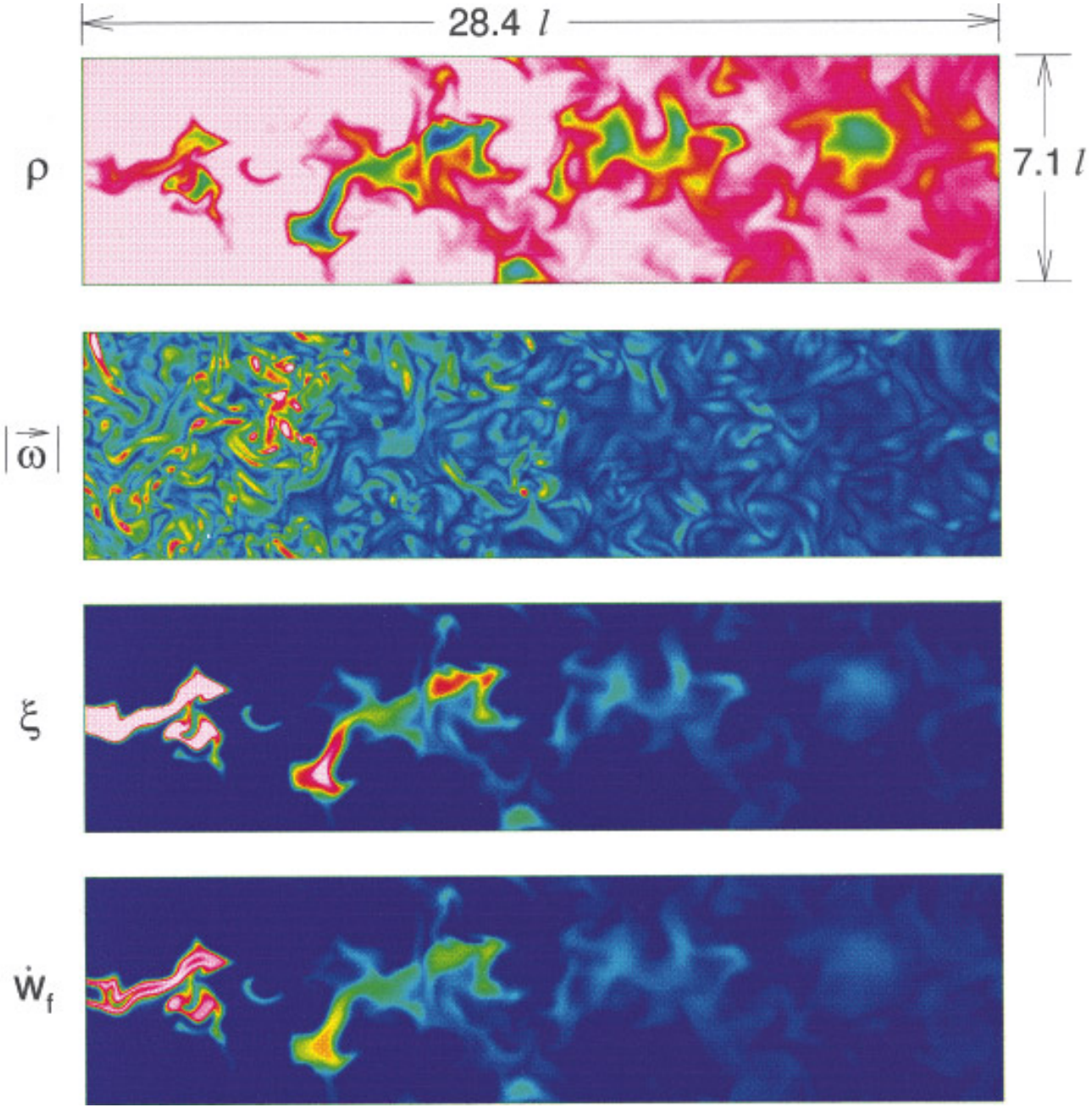

FIG. 3. Contours of density, vorticity-magnetude, mixture-fraction, and reaction rate on a centerline slice from case D.

Figure 9 shows the downstream growth of the Taylor microscales, where a microscale in the i direction is computed as

$$\lambda_i = \left[\frac{\langle u_i^2\rangle}{\langle(\partial u_i/\partial x_i)^2\rangle}\right]^{1/2} \text{(no sum on } i\text{)}, \qquad (43)$$

$$\langle(\,)\rangle \equiv \int_0^1\int_0^1\int_0^1 (\,)\,dydzdt.$$

The length scales drop slightly, as the inlet flow adjusts to its environment, then they rise steadily up to the exit. The curves show that the turbulence is roughly isotropic. By assuming high Reynolds number and a power-law decay for the turbulent kinetic energy, the turbulence energy budget predicts that, with no heat release, all length scales should grow as $(x/l)^{1/2}$ [45]. The coefficient 0.0156, as well as coefficients for theoretical curves in subsequent plots, were determined by a visual fit to the data. It can be seen

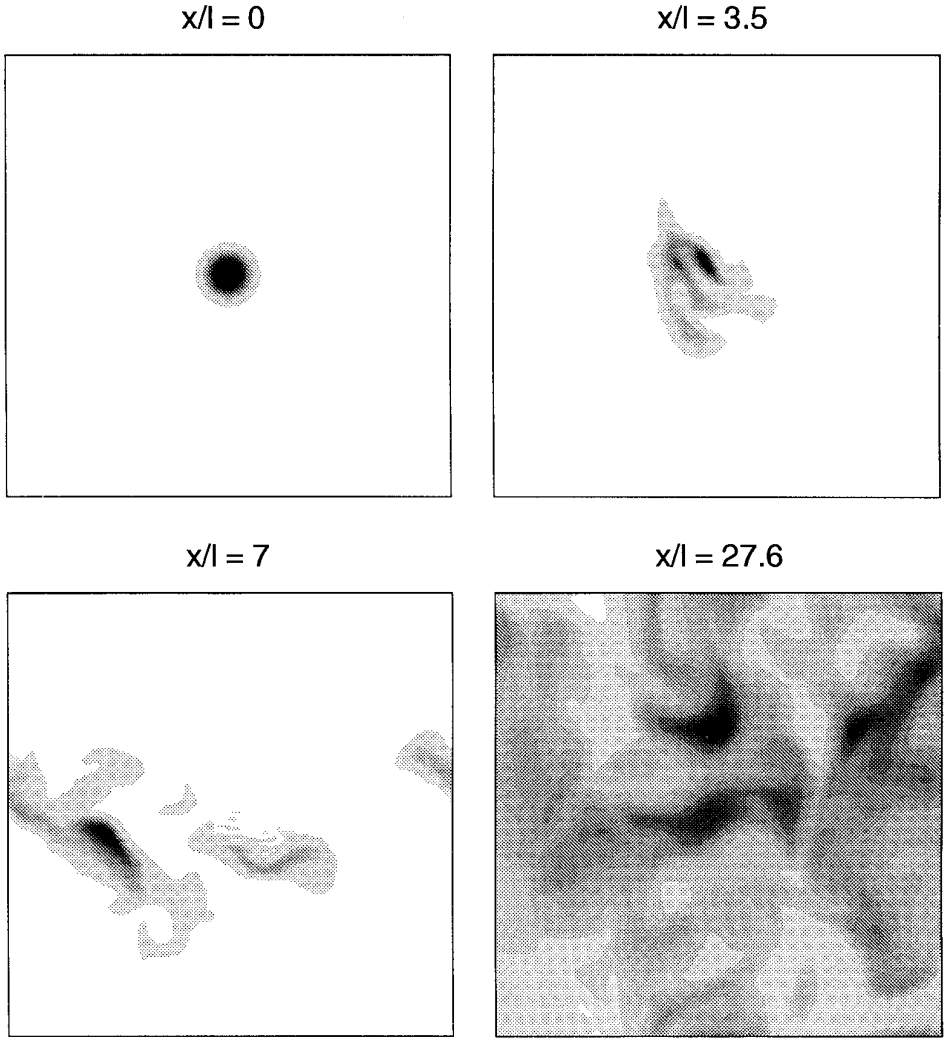

FIG. 4. Gray-scale contours of mixture-fraction on various cross-stream cuts, taken from case A.

from the plots that the heat release has little effect on the growth of the Taylor microscales. Figure 10 shows the power law decay of turbulent kinetic energy. The straight line corresponds to the empirical decay law of $(x/l)^{1.25}$ reported by Comte-Bellot and Corrsin [46] for grid turbulence in a wind tunnel. The results show that, after some initial development, the simulated turbulent decay approximates the experimental data. Again, the decay of velocity fluctuations is nearly the same for all four cases. This insensitivity of velocity statistics to density variations was also demonstrated in Sandoval's simulations [33]. Figure 11 is a plot of the Taylor–Reynolds numbers versus downstream distance. In the plots, R_λ is defined for each direction, i.e.,

$$R_{\lambda,i} = \frac{\lambda_i \sqrt{\langle u_i^2 \rangle}}{\nu} \text{ (no sum on } i\text{)}.$$

The Taylor–Reynolds numbers decrease downstream but remain high enough so that each case may be considered turbulent throughout the domain [13].

14.2. *Plume*

Figure 12 depicts the decay of the mean value of ξ along the plume centerline as a function of initial large-eddy turnover time. The mean was computed by taking a time average of grid points within a distance of four grid spaces from the plume centerline. Brown and Bilger [27] report a decay law of t_{le}^{-1} and the plot shows that $\langle \xi^c \rangle$, from case A, decays as t_{le}^{-1} with an error bound of $100(|\langle \xi^c \rangle - 0.08/t_{le}|/0.08/t_{le}) < 18\%$. The line corresponding to t_{le}^{-1} is not meant to imply that there was no scatter in the experimental data. The experimental scatter is not shown here for clarity. The other three cases appear to follow the same

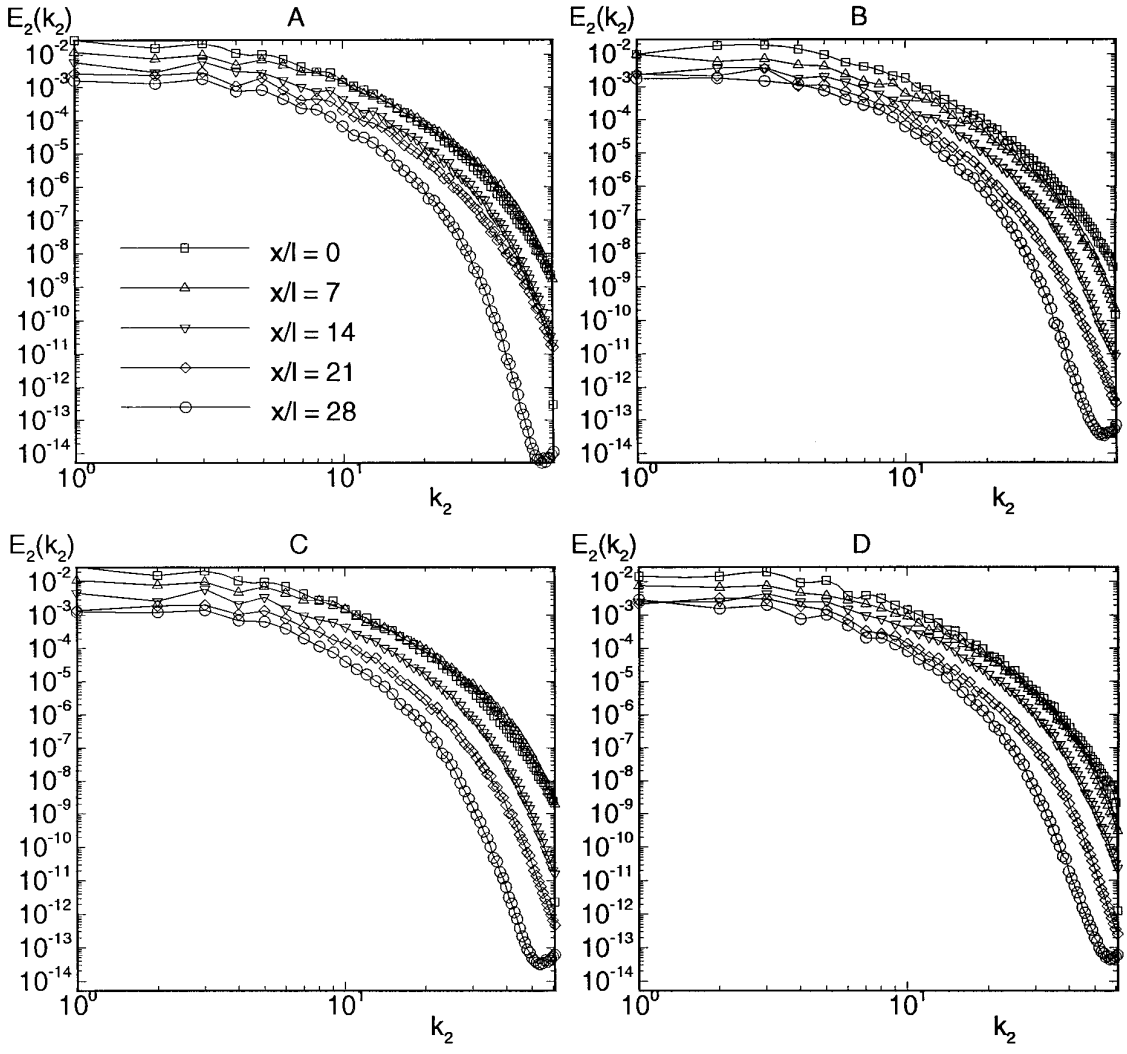

FIG. 5. Two-dimensional total energy spectra at various downstream locations.

trends as case A, e.g., rising and falling in the same places. This is likely due to the fact that the inlet flow was the same for all four cases and heat release did not have a large effect on the flow. In Fig. 13 is plotted the decay of the root-mean-square value of ξ along the plume centerline. Brown and Bilger find an empirical decay law of $t_{\mathrm{le}}^{-1.32}$ and from the plot it can be determined that, after one large eddy turnover, ξ^c_{rms} for case A approximates the experimental data with an error bound of $100(|\xi^c_{\mathrm{rms}} - 0.09/t_{\mathrm{le}}^{1.32}|/0.09/t_{\mathrm{le}}^{1.32}) < 37\%$. From random sampling theory, it is expected that the statistical scatter in the second moment of ξ^c will be greater than the error in the first moment.

Figure 14 shows the downstream growth of the standard deviation σ of the mean scalar profile, computed as follows: first, $\langle\xi(r, t_{\mathrm{le}})\rangle$ is computed at each downstream (eddy-time) location by averaging in time and over annular regions at specific radial positions; then σ is computed via numerical integration as

$$\sigma(t_{\mathrm{le}}) = \left(\frac{\int_0^{L/2} r^2\langle\xi(r, t_{\mathrm{le}})\rangle\, dr}{\int_0^{L/2}\langle\xi(r, t_{\mathrm{le}})\rangle\, dr}\right)^{1/2}.$$

The plume's spread is very close to the $t_{\mathrm{le}}^{1/2}$ dependence expected from (i) the conservation of mixture fraction, (ii) an assumption of self-similar radial profiles for $\langle\xi\rangle$, and (iii) $\langle\xi^c\rangle$ having a decay exponent of -1. Brown and Bilger [27], Nakamura *et. al.* [26], and Komori and Ueda [47] all report growth exponents of 1/2. Some of the discrepancy in the plot may be due to the limited distance from the plume centerline to the side boundaries, which the plume eventually crosses.

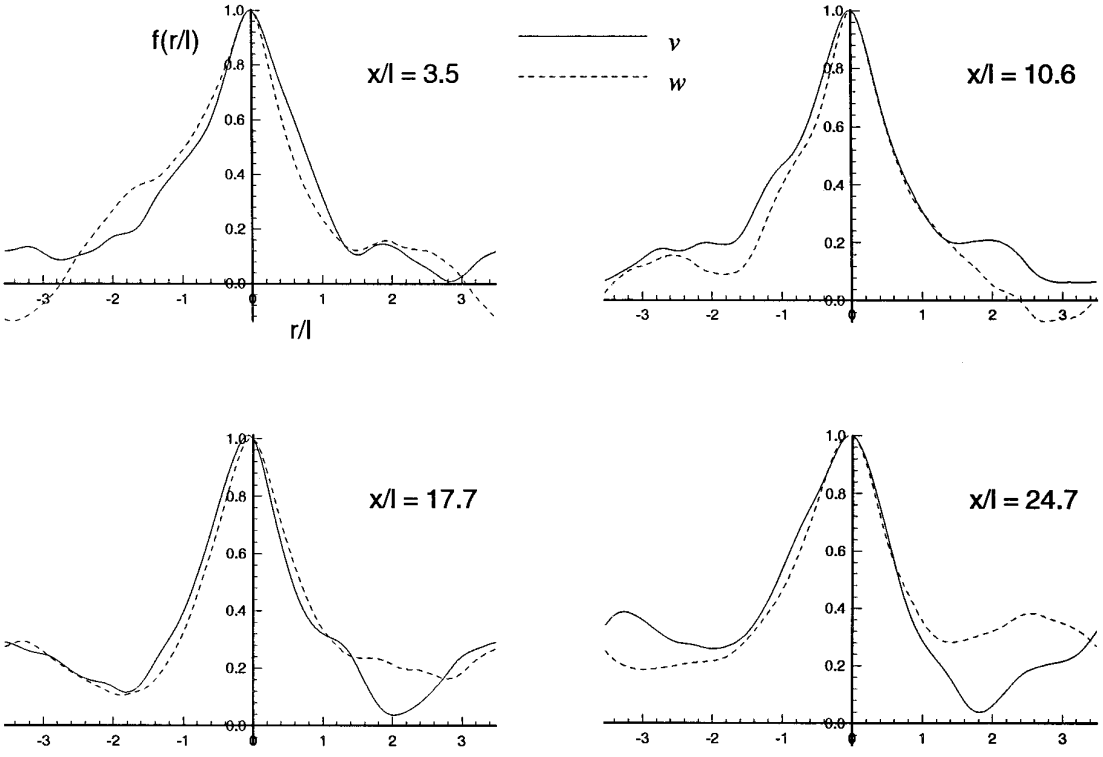

FIG. 6. Longitudinal velocity autocorrelations from case A.

14.3. *Reactive Scalar*

The centerline decay of the mean (time-averaged) fuel mass fraction is plotted in Fig. 15. Since the inlet concentrations differ from the Brown and Bilger experiment, a direct comparison cannot be made. For case A, the reaction is seen to occur approximately midway between the frozen and equilibrium chemistry limits. In the frozen limit $Y_f = Y_{f1}\xi$, while in the equilibrium chemistry limit

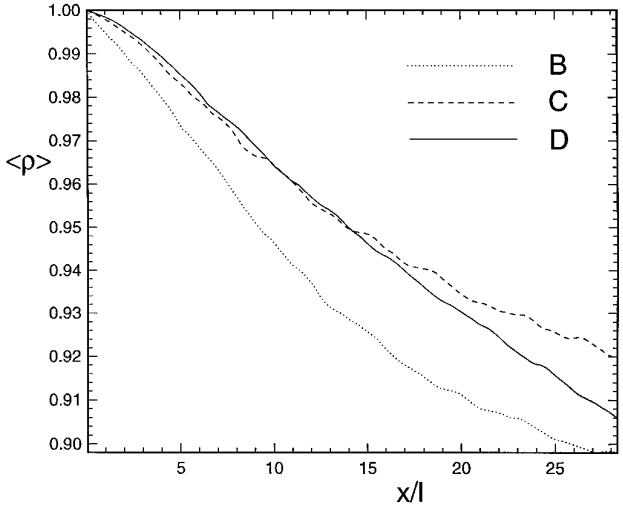

FIG. 7. Mean density versus downstream distance.

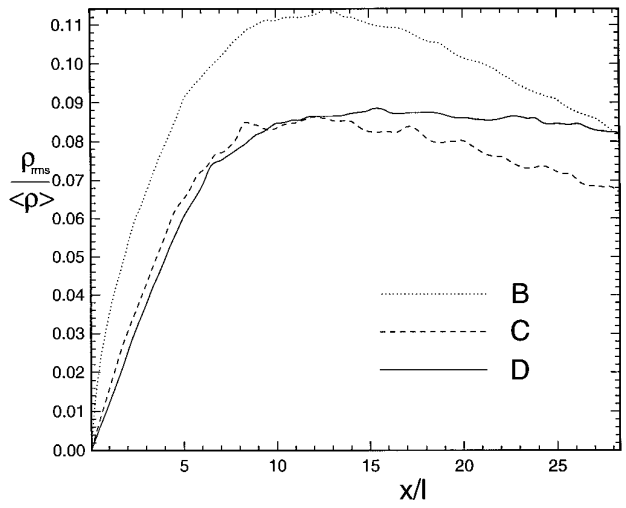

FIG. 8. Density fluctuations versus downstream distance.

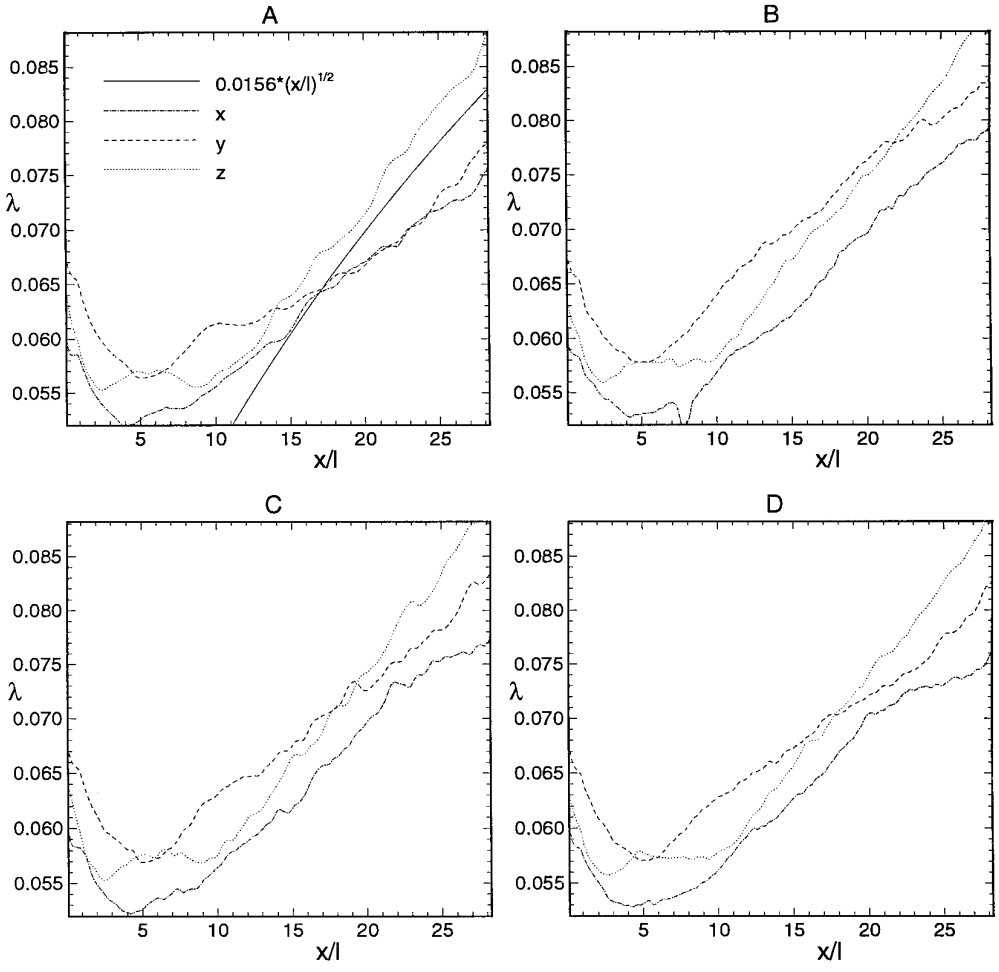

FIG. 9. Taylor microscales versus distance downstream.

$$Y_f = \begin{cases} 0 & \text{if } \xi \le \xi_{\text{st}} \\ Y_{f1}\dfrac{\xi - \xi_{\text{st}}}{1 - \xi_{\text{st}}} & \text{if } \xi > \xi_{\text{st}} \end{cases}$$

From cases C and D it can be seen how an increase in the activation temperature moves the reaction towards the frozen limit.

The root-mean-square of the centerline fuel mass fraction normalized by the mean value is plotted in Fig. 16. It is interesting to note that the limits cross at approximately one large eddy turnover time. Unlike $\langle Y_f^c \rangle$, $Y_{f,\text{rms}}^c$ may lie outside the frozen and equilibrium limits and these limits may cross each other. This behavior is due to the triple correlation terms in the conservation equation for the scalar variance [48]. For $t_{\text{le}} > 1$ the reacting flow data lie between the frozen and equilibrium limits, but near the inlet they appear to follow the frozen chemistry curve. Case D is very near the frozen limit until far downstream.

Figure 17 shows the mean centerline reaction rate versus large-eddy turnover time. For cases A, B, and C a rapid drop occurs near a time of 3, as the fuel is fully consumed. The low Damköhler number and high activation temperature of case D result in a slow rate of reaction, compared to the other cases.

14.4. *Extinction*

The strength of the reaction is measured by examining its proximity to the extinction regime. The conditions for the extinction of a diffusion flame were first derived by Liñán [49] using activation-energy asymptotics. Williams [50] defines quenching criteria using a reduced Damköhler number, which is given in terms of current variables,

$$\text{Da}_e \equiv \text{DaPe}(r\xi_{\text{st}} Y_{f1} e^{-T_a/T_f}) \left[\frac{T_f^2}{T_a(T_f - 1)}\right]^3 [2\xi_{\text{st}}(1 - \xi_{\text{st}})]^2 \left(\frac{\rho}{D\,\nabla\xi \cdot \nabla\xi}\right)|_{\xi=\xi_{\text{st}}}, \tag{44}$$

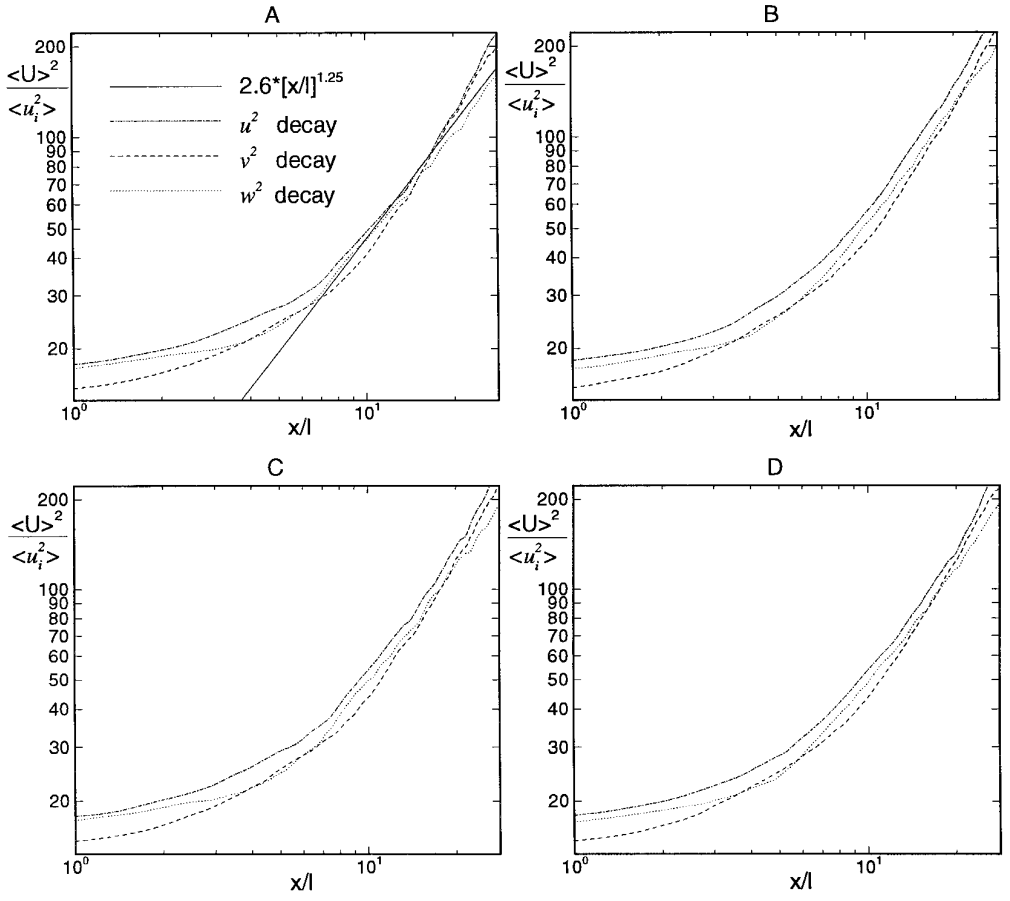

FIG. 10. Centerline decay of turbulent kinetic energy.

where T_f is the adiabatic flame temperature, given by

$$T_f = \frac{Y_{o2} + rY_{f1} + Y_{f1}Y_{o2}\, q(\gamma - 1)/\gamma}{Y_{o2} + rY_{f1}}. \tag{45}$$

Extinction will occur when $\mathrm{Da}_e \leq \mathrm{Da}_E$, where

$$\mathrm{Da}_E = [(1 - |\psi|) - (1 - |\psi|)^2 + 0.26(1 - |\psi|)^3 + 0.055(1 - |\psi|)^4]e. \tag{46}$$

If the temperatures of the fuel and oxidizer streams are equal, as in the present cases, then $\psi = 2\xi_{\mathrm{st}} - 1$; thus $\mathrm{Da}_E = 0.478$. Equations (44) and (46) provide the criteria for local flamelet extinction. The subscript $\xi = \xi_{\mathrm{st}}$ indicates that Da_e is to be evaluated on the stoichiometric surface. It can be seen that if the quantity $(D/\mathrm{Pe})\,\nabla\xi\cdot\nabla\xi$, defined as the scalar dissipation rate, becomes too large, then extinction will occur. The scalar dissipation rate is approximately proportional to the square of the local strain rate, hence sufficiently large strain rates cause quenching of flamelets. Figure 18 is a scatter plot of Da_e at locations very near ξ_{st}. The data were taken from case D because the reaction for this case is closest to the extinction limit. The plot indicates that no flame quenching should be occurring.

15. CONCLUSIONS

This work has established a method for simulating a reactive plume in spatially developing, grid turbulence. By applying a low Mach number approximation to the fully compressible Navier–Stokes equations, the computing time needed to integrate the governing equations is reduced by roughly a factor of 1/M. A high degree of parallel efficiency was achieved by decomposing the three-dimensional computational domain into planar sections. The compact scheme for computing spatial derivatives is a good alternative to spectral methods when the boundaries are nonperiodic. The global nature of the compact scheme makes it sensitive to the boundary conditions. For the turbulent inflow and outflow boundaries of the simulation, a fifth-order compact boundary scheme was developed and found to be stable. In solving the pressure Poisson equa-

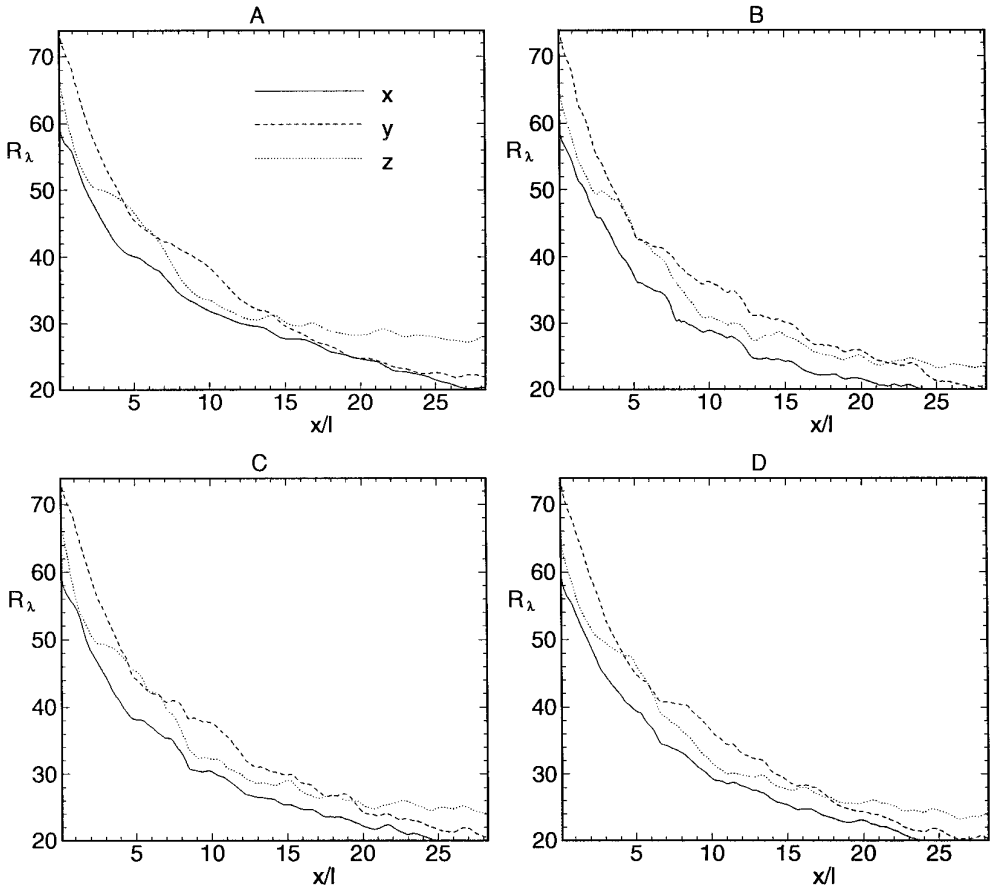

FIG. 11. Taylor–Reynolds numbers versus distance downstream.

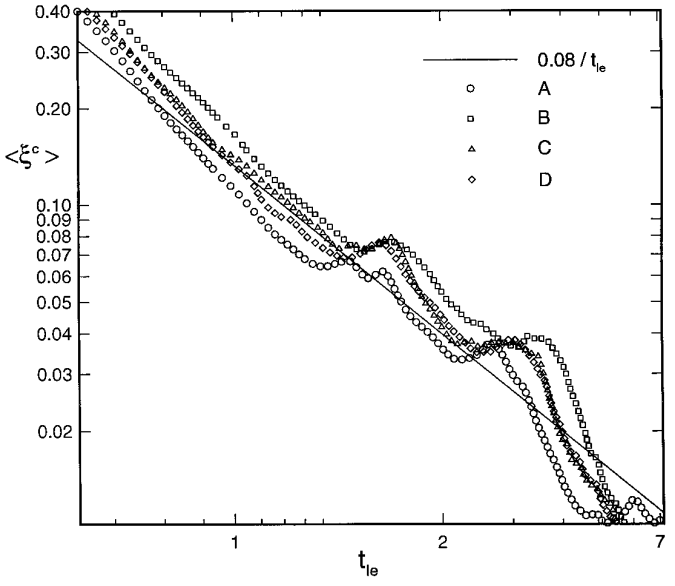

FIG. 12. Mean mixture fraction along centerline.

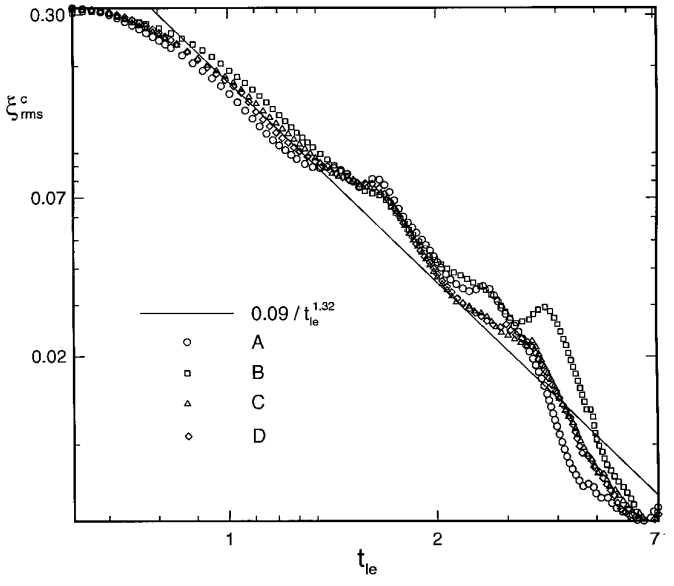

FIG. 13. RMS of mixture fraction along centerline.

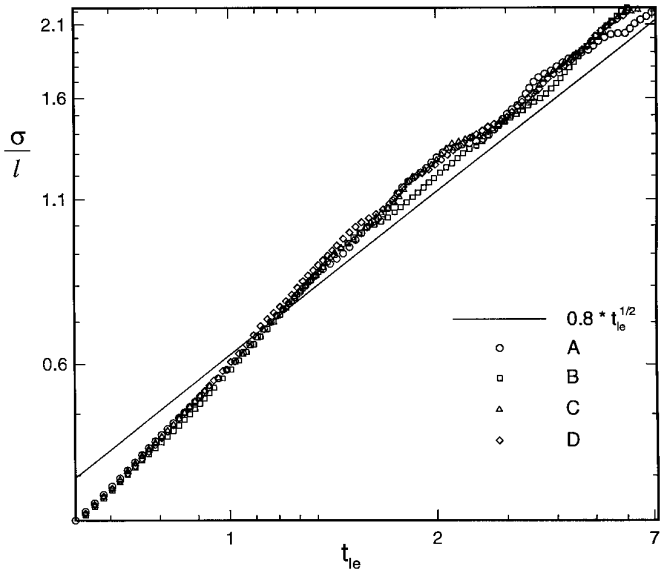

FIG. 14. Standard deviation of mean scalar profile versus large eddy turnover time.

tion, a second-order approximation to the density time derivative was found to be significantly more stable (allowing larger density variations) than a third-order approximation. The third-order Adams–Bashforth time-stepping algorithm was found to be stable for maximum density changes up to about a factor of 3. For higher density ratios, a predictor–corrector method such as second- or third-order Runge–Kutta should be used [34].

The technique of introducing mature turbulence at the inlet removes the need for a lengthy computational region in which turbulence must develop. Since the inlet turbulence is specified by scanning through an existing three-dimensional turbulent field, the interpolation between grid points (of the inlet field) can affect the solution. Linear interpolation was found to be unacceptable since it results in discontinuous velocity derivatives, thereby causing the pressure term in the mechanical energy equation to oscillate. Cubic-spline interpolation produces inlet velocities with continuous derivatives and was found to help stabilize the calculation. A one-dimensional advective exit condition for the primitive variables, along with a Neumann/Dirichlet pressure condition at the inflow/outflow bound-

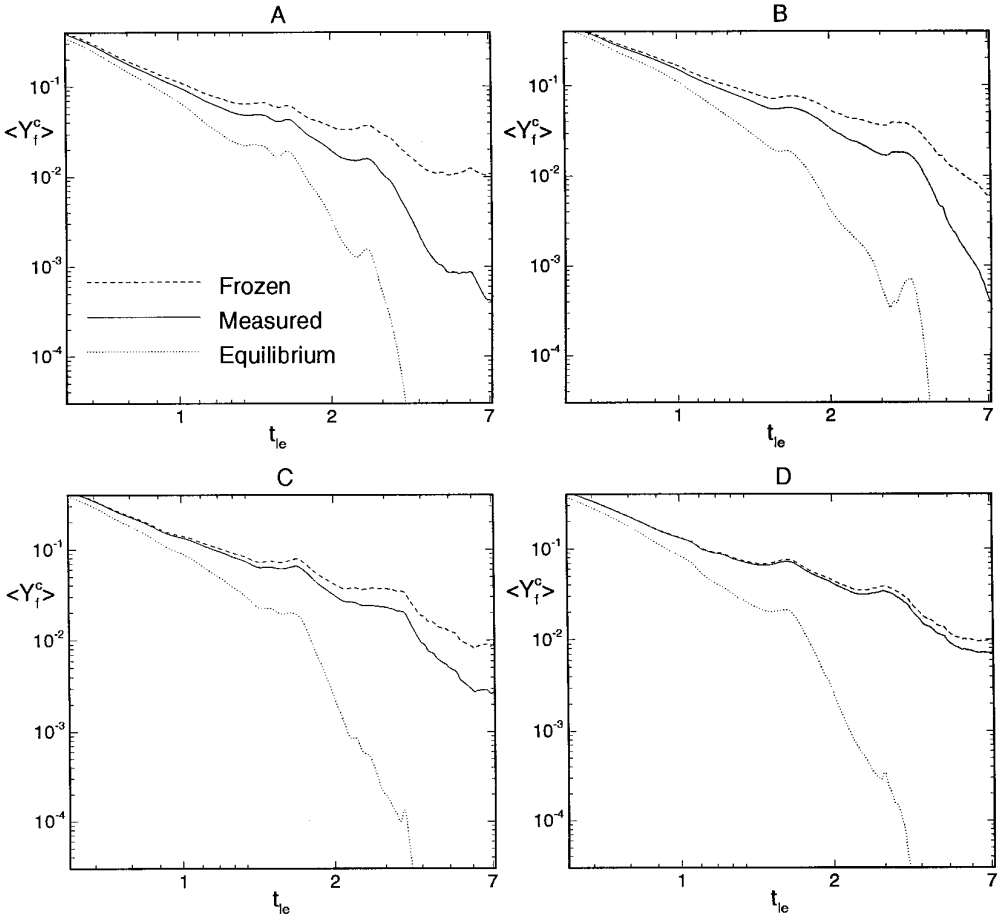

FIG. 15. Mean and limiting values of fuel mass fraction along centerline.

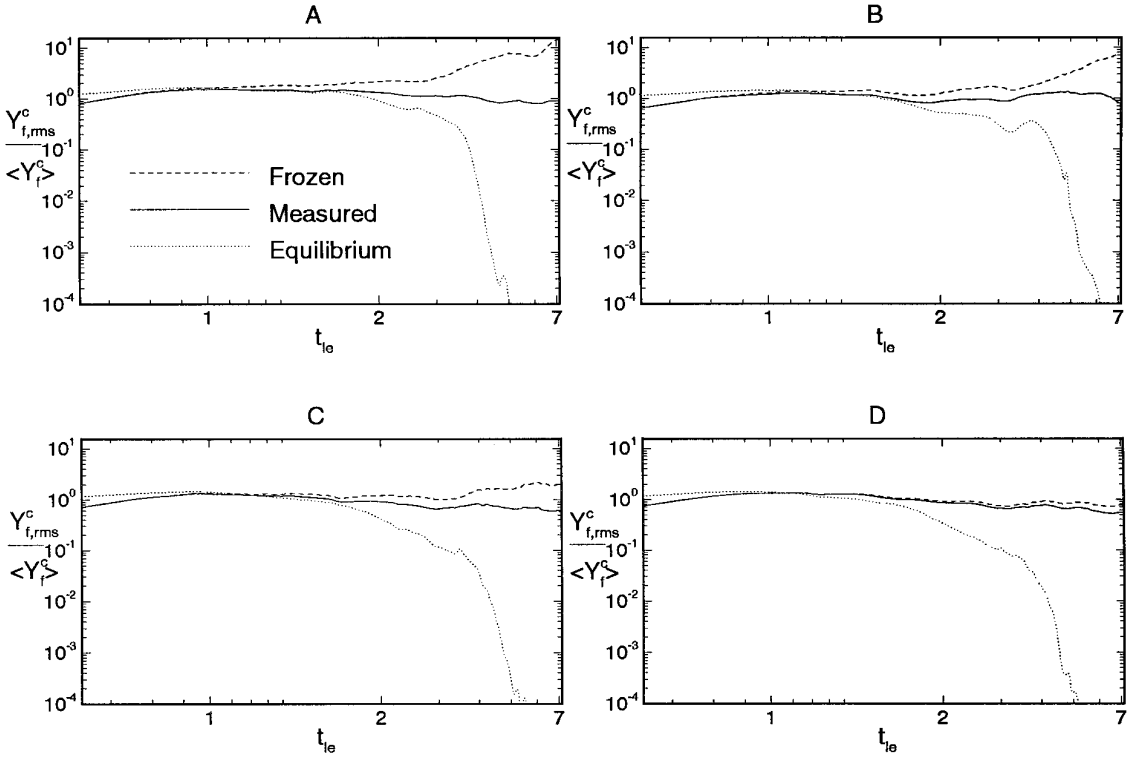

FIG. 16. Fluctuation of fuel mass fraction along centerline.

aries, was found to work well. The open nature of the streamwise boundaries allows for global expansion of the fluid due to chemical heat release. This allows the thermodynamic pressure (but not the dynamic pressure) to be assumed constant, which is the case in combustors vented to the atmosphere.

For the incompressible simulation, the downstream growth of Taylor microscales approximately followed the $\frac{1}{2}$ power law predicted from the turbulence energy budget. The decay of turbulent kinetic energy roughly followed the 1.25 empirical power law reported by Comte-Bellot and Corrsin. The centerline decay of mixture-fraction was in fair agreement with a -1 power law reported by Brown and Bilger. The centerline decay of the scalar rms also

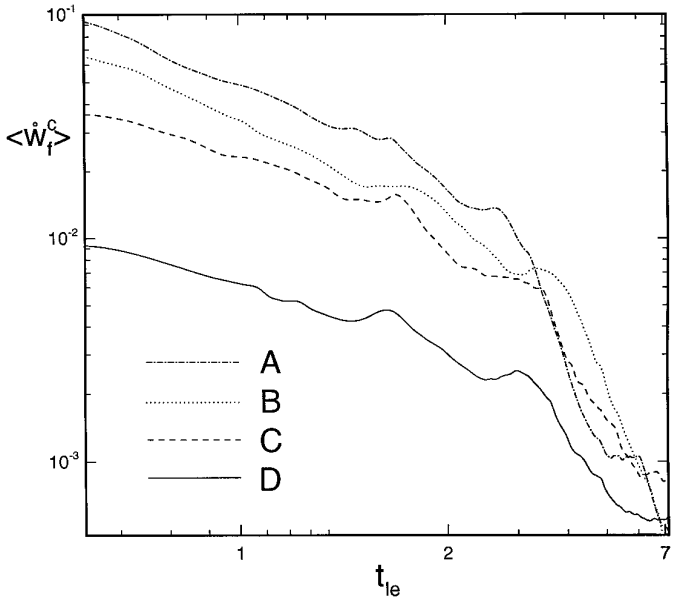

FIG. 17. Mean centerline reaction rate.

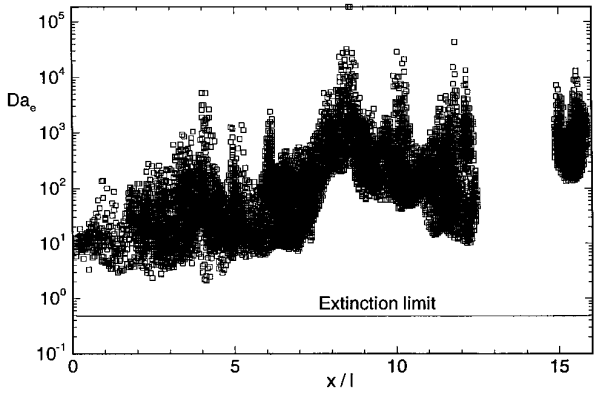

FIG. 18. Reduced Damköhler number at stoichiometric locations for case D.

agreed with Brown and Bilger's reported 1.32 power law, albeit with a larger error bound. Furthermore, the spread of the plume agreed quite closely with a $\frac{1}{2}$ power law predicted from self-similarity. The density dilatation in the exothermic simulations was seen to have little effect on the velocity statistics. Increasing the activation temperature moved the reaction toward the frozen limit as expected.

Resolution requirements of DNS restrict the range of turbulence and chemistry parameters that can be achieved; however, much of the important physics observed in experiments of grid turbulence was also observed here. Regarding the chemistry, it is doubtful whether DNS can be used to compute turbulent reacting flows with very low values of ξ_{st}, e.g., as with methane–air combustion. However, the primary purpose of DNS is to investigate the physics of turbulent flows so as to gain understanding that may be used to improve turbulence models used in engineering codes. In this context, the methodology presented herein may be considered as an additional tool for investigating the physics of turbulent reacting flows in open domains.

ACKNOWLEDGMENTS

This work was supported by NSF under Grant CTS-9415280 and utilized the Connection Machine Model-5 at the National Center for Supercomputing Applications, University of Illinois at Urbana-Champaign. Additionally, we wish to thank Dr. W. E. Mell for providing the inlet data fields, Dr. D. N. Slinn and Dr. A. Almgren for advice on the coding, and Professor George Kosály for useful discussions and suggestions.

REFERENCES

1. J. J. Riley, R. W. Metcalfe, and S. A. Orszag, *Phys. Fluids* **29,** 406 (1986).
2. P. A. McMurtry, W.-H. Jou, J. J. Riley, and R. W. Metcalfe, *AIAA J.* **24**(6), 962 (1986).
3. P. Givi, W.-H. Jou, and R. W. Metcalfe, "Flame Extinction in a Temporally Developing Mixing Layer," in *Proceedings, 21st Symposium (International) on Combustion* (The Combustion Institute, Pittsburgh, PA, 1986).
4. A. D. Leonard and J. C. Hill, AIAA Paper 87-0134, Jan. 1987 (unpublished).
5. W. H. Jou and J. J. Riley, *AIAA J.* **27**(11), 1543 (1989).
6. D. B. Haidvogel, A. R. Robinson, and E. D. Schulman, *J. Comput. Phys.* **34,** 1 (1980).
7. P. Peyret and T. D. Taylor, *Computational Methods for Fluid Flows* (Springer-Verlag, New York/Berlin, 1983).
8. K. Z. Korczak and A. T. Patera, *J. Comput. Phys.* **62,** 361 (1986).
9. N. K. Ghaddar, G. E. Karniadakis, and A. T. Patera, *Numer. Heat Transfer* **9,** 277 (1986).
10. H. C. Yee, *J. Comput. Phys.* **68,** 151 (1987).
11. F. F. Grinstein, *J. Comput. Phys.* **115,** 43 (1994).
12. J. H. Chen, S. Mahalingam, I. K. Puri, and L. Vervish, "Effect of Finite-Rate Chemistry and Unequal Schmidt Numbers on Turbulent Non-Premixed Flames Modeled with Single-Step Chemistry," in *The WSS/CI Fall Meeting, Berkeley, California, October 12, 1992.*
13. K. K. Nomura and S. E. Elghobashi, *Phys. Fluids A* **4,** 606 (1992).
14. C. J. Montgomery, G. Kosály, and J. J. Riley, *Combust. & Flame* **95,** 247 (1993).
15. T. J. Poinsot and S. K. Lele, *J. Comput. Phys.* **101,** 104 (1992).
16. S. K. Lele, *J. Comput. Phys.* **103,** 16 (1992).
17. S. Lee, S. K. Lele, and P. Moin, *Phys. Fluids A* **3,** 657 (1991).
18. J. C. Buell, *J. Comput. Phys.* **95,** 313 (1991).
19. T. A. Zang, J. P. Drummond, G. Erlebacher, C. Speziale, and M. Y. Hussaini, AIAA Paper, 87-0130, January 1987 (unpublished).
20. S. Lee, S. K. Lele, and P. Moin, *Phys. Fluids A* **4,** 1521 (1992).
21. H. Le and P. Moin, Stanford Report No. TF-58, December 1994 (unpublished).
22. R. Friedrich and M. Arnal, *J. Wind Eng. Ind. Aerodyn.* **35,** 101 (1990).
23. G. I. Taylor, *Proc. R. Soc. London Ser. A* **164,** 476 (1938).
24. W. R. Mickelsen, *J. Fluid Mech.* **1,** 397 (1960).
25. M. Gad-El-Hak and J. B. Morton, *AIAA J.* **12,** 558 (1979).
26. I. Nakamura, Y. Sakai, and M. Miyata, *J. Fluid Mech.* **178,** 379 (1987).
27. R. J. Brown, and R. W. Bilger, *J. Fluid Mech.,* in press.
28. R. W. Bilger, "Turbulent Flows with Nonpremixed Reactants," in *Topics in Applied Physics*, **Vol. 44,** edited by P. A. Libby and F. A. Williams (Springer-Verlag, Berlin, 1980), Chap. 3.
29. N. Peters, *Prog. in Energy and Combust. Sci.* **10,** 319 (1984).
30. R. W. Bilger, *Phys. Fluids A* **5,** 436 (1993).
31. D. A. Anderson, J. C. Tannehill, and R. H. Pletcher, *Computational Fluid Mechanics and Heat Transfer* (Hemisphere, Washington, DC, 1984).
32. D. R. Durran, *Mon. Weather Rev.* **119**(3), (1991).
33. D. L. Sandoval, Ph.D. theisis, University of Washington, 1995 (unpublished).
34. H. N. Najm, *AIAA J.*, submitted.
35. A. J. Chorin, *J. Comput. Phys.* **2,** 2 (1967).
36. P. M. Gresho, *Int. J. Numer. Methods Fluids* **11,** 587 (1990).
37. W. E. Mell, V. Nilsen, G. Kosály, and J. J. Riley, *Combust. Sci. Technol.* **91,** 179 (1993).
38. D. R. Durran, M.-J. Yang, D. N. Slinn, and R. G. Brown, *Mon. Weather Rev.* **121**(2), (1993).
39. J. C. Buell and P. Huerre, "Inflow/Outflow Boundary Conditions and Global Dynamics of Spatial Mixing Layers," in *CTR Proceedings, Summer Program*, 1988.
40. P. S. Lowery and W. C. Reynolds, Stanford Report No. TF-26, September 1986 (unpublished).
41. R. Prosser, private communication, 1996.
42. J. J. Dongarra, Report No. CS-89-85, Computer Science Department, University of Tennessee and Mathematical Sciences Section, Oak Ridge National Laboratory, 31 January 1994 (unpublished).
43. S. Corrsin, "Turbulence: Experimental Methods," in *Handbuch der Physik*, **Vol. VIII/2,** (edited by C. Truesdell) (Springer-Verlag, New York/Berlin, 1963).
44. K. K. Nomura and S. E. Elghobashi, *Theoret. Comput. Fluid Dyn.* **5,** 153 (1993).
45. H. Tennekes and J. L. Lumley, *A First Course in Turbulence* (MIT Press, Cambridge, MA, 1972).
46. G. Comte-Bellot and S. Corrsin, *J. Fluid Mech.* **48,** 273 (1971).
47. S. Komori and H. Ueda, *Phys. Fluids A* **27,** 77 (1984).
48. R. J. Brown, private communication, 1995.
49. A. Liñán, *Acta Astronaut.* **1,** 1007 (1974).
50. F. A. Williams, *Combustion Theory*, 2nd ed. (Addison–Wesley, Reading, MA, 1985).